SPLIT RING RESONATOR AND METAMATERIALS AT MICROWAVE REGIME, NUMERICAL ANALYSIS, DESIGN, CHARACTERIZATION

by

Seyedehayda Sadeghzadeh

B.S., Electrical and Electronics Engineering, Tabriz University, 2007

Submitted to the Institute for Graduate Studies in

Science and Engineering in partial fulfillment of

the requirements for the degree of

Master of Science

Graduate Program in Electrical and Electronics Engineering

Bogazici University

2012

SPLIT RING RESONATOR AND METAMATERIALS AT MICROWAVE REGIME

NUMERICAL ANALYSIS, DESIGN, CHARACTERIZATION

APPROVED BY:

Asst.Prof. Arda Deniz Yalçınkaya . . . .

(Thesis Supervisor)

Prof. Cengizhan Öztürk . . . .

Asst. Prof. Hamdi Torun . . . .

DATE OF APPROVAL: 28.08.2012

ACKNOWLEDGEMENTS

ABSTRACT

SPLIT RING RESONATOR AND METAMATERIALS AT MICROWAVE REGIME, NUMERICAL ANALYSIS, DESIGN, CHARACTERIZATION

Recently, there has been a significant interest in Terahertz (THz) technology, primarily for its potential applications in detection of concealed objects as well as in medical imaging for non-invasive diagnostics. THz spectrum lies between the infrared and microwave spectra. The artificially structured frequency selective devices have been demonstrated to overcome a significant bottleneck in THz band. Among different Metamaterial configurations, Split Ring Resonator (SRR) can be used to create compact narrowband wave plates at THz frequencies, which is variable by changing the radius of ring, number of rings, material thickness, size of gaps. In this work we have designed double-ring SRR structures in four different sizes to achieve various resonance frequencies in the microwave band. For simplicity, SRR prototypes are designed in mm-size resulting resonance peaks at 3.7 GHz, 4.3 GHz, 5.9 GHz and 7.4 GHz for ring diameters of 4 mm, 3.6 mm, 3 mm and 2.6 mm, respectively. By calculating the capacitance and inductance of rings, the resonance frequency can be calculated mathematically. The fabricated split ring resonator prototypes are placed between two antennas and experimental characterization is done by a vector network analyzer in both of the finite-element simulation and experiments we have inspected Transmission (S21) and Reflection (S11) coefficients. We are characterizing samples with backside metallization. Simultaneous minimization of transmission and reflection at a certain frequency band, play a crucial role in obtaining high absorption coefficient. We employ the same design methodology for the design of THz absorbers.

ÖZET

KESİK HALKA RESONATÖRÜ VE METAMALZEMELER

İnvazif olmayan tıbbi görüntüleme, saklı silahların algılanması gibi farklı uygulama alanlarında son zamanlarda yoğun olarak kullanılmaya başlanan Terahertz (THz) teknolojisi bilimi dünaysının da üzerinde artan bir oranda araştırma yaptığı bir konudur. THz frekans spektrumu, mikrodalga bandı ile kızılötesi bandı arasında yer alan yaklaşık 0.1 THz ile 10 THz arasını kapsamaktadır. Bu frekans bandında salınan fotonların iyonize olmayan, düşük enerjili parçacılar olması THz teknolojisini algılama açısında avantajlı kılmaktadır. Tasarlanmış malzemelerin THz frekans bandında çalışması ile THz boşluğu olarak bilinen bant doldurulmuş olmaktadır. Metamalzemeler olarak bilinen konfigürasyonlar, dar bir frekans bandında solak özellik göstermektedir ve bu tür yapılar kesikli halka rezonatörlerinin geometrileri tasarım parametresi olarak kullananılarak oluşturulmaktadır. Bu çalışmada, ikili kesik halka rezonatörü kullanarak, dört farklı tasarım için 3.7 GHz, 4.3 GHz, 5.9 GHz ve 7.4 GHz için rezonans frekansı sırsıyla 4 mm, 3.6 mm, 3 mm ve 2.6 mm halka çapı ile elde edilmiştir. Halka aygıtlar için eşdeğer endüktans ve sığa değerleri hesaplanmış, ve bu değerler kullanılarak rezonans frekansları bulunmuştur. Üretilen prototipler iki anten arasına yerleştirilmiş ve çift yönlü dağılmış s-parametrelerinin ölçümleri ile iletim (S21) ve yansıma (S11) karakteristikleri çıkarılmıştır. Mikrodalga ölçümleri hem arka kısmı metalizasyonlu hem de metalizasyonsuz aygıtlar için yapılmıştır. Rezonatör yapılarının yüksek soğurma gösterebilmesi için gerek yansıma, gerekse de iletim katsayılarının ilgili rezonans frekansında minimizasyonu için tasarım yapılmıştır. Mikrodalga frekansındaki bu tasarım yöntemi THz soğurucu yapılarına da uyarlanmıştır.

TABLE OF CONTENTS

LIST OF FIGURES

LIST OF TABLES

LIST OF SYMBOLS

$\vec{E}$	Electric Field
$\vec{H}$	Magnetic Field
$\vec{D}$	Electric flux density
$\vec{B}$	Magnetic flux density
$\vec{k}$	Propagation constant
$\vec{S}$	Energy flow
n	Refractive index
R	Reflection coefficient
T	Transmission coefficient
Absorption	Absorption
n_e	Density of electrons
e	Electric charge
m_e	Effective mass of the electron
a	Lattice constant
r	Radius of wires
d	Distance between two rings
w	Width of ring
R_{in}	Radius of inner ring
R_{out}	Radius of outer ring
g	Gap (width of split in each ring)
c_0	Speed of light
L	Ring inductance
C	Capacitance
$K_{1/2}$	Constants related to properties of materials
A	Cross-sectional area
l	Effective length of ring
t	Thickness of metallic layer
f	frequency
$R_{/}$	radius of inner or outer ring (R_{in} or R_{out})

C_{mut}	Mutual capacitance
C_{surf}	Surface capacitance
C_{gap}	Gap capacitance
$C_{overall}$	Total lumped capacitance for a ring
r_0	Quadrant of width of ring
M	Mutual inductance
$a_{1,2}$	Average radius of inner or outer ring
C_1, C_2	Lumped capacitances for inner and outer rings
L_1, L_2	Lumped inductances for inner and outer rings
R_c	Conductor loss
R_d	Dielectric loss
$\tan \alpha$	Loss tangent of substrate
h	Substrate thickness
V_1	Voltage across port one
V_2	Voltage across port two
I_1	Current through pass port one
I_2	Voltage through pass port one
Z_0	Characteristic impedance
S_{11}	Input port voltage reflection coefficient
S_{22}	Output port voltage reflection coefficient
S_{12}	reverse voltage gain
S_{21}	forward voltage gain
C_f	Fringing capacitance
s	Gap width
ε	Permittivity
μ	Permeability
ε_{eff}	Effective or relative permittivity
ε_0	Free-space (vacuum) permittivity
μ_{eff}	Effective relative permeability
μ_0	Free-space (vacuum) permeability
ρ	Electric charge density
ω	Angular frequency

θ	Incident angle
θ'	Refractive angle
ω_p	Plasma frequency
γ_d	Damping (collision) frequency
σ	Conductivity
ξ	Small parameter (<0.25)
ω_m	Resonance frequency
δ	Skin depth

LIST OF ACRONYMS/ABBREVATIONS

RHM	Right Handed Material
LHM	Left Handed Material
SRR	Split Ring Resonator
EM	Electro-Magnetic field
RLC	Resistor, Inductance, Capacitance
EEMR	Electric Excitation coupled with Magnetic Resonance
DSRR	Double Split Ring Resonator
NIM	Negative Index Material
FDTD	Finite Difference Time Domain
PEC	Perfect Electric Conductor
PMC	Perfect Magnetic Conductor
PML	Perfectly Matched Layer
VNA	Vector Network Analyzer
TE	Transverse Electric
TM	Transverse Magnetic

1. INTRODUCTION

1.1. Left Handed-Materials: Concept

In 1968 V. G. Veselago' s idea [1] showed that it is possible to have material with negative refractive indices which comes from negative permittivity and negative permeability simultaneously. As those kinds of material are not found in the nature it could not be modeled practically till 1990. 20 years ago, Sir J. B. Pendry proposed artificially designed a structure [2] that can achieve negative permeability. It makes Veselago's idea true. He predicts that the Left Handed Material (LHM) comes from the left handed material orthogonal set which is in reverse relation with Right Handed Material vector system [3] . The $\vec{E}$, electric field and $\vec{H}$, magnetic field and $\vec{k}$ vector obey LHM vector system. This can refer to Negative Index Material (NIM) [4] which has negative permittivity, ε and negative permeability, μ and negative refractive index, n in a certain frequency band.

1.1.1. Mathematical Modeling of Metamaterial

In this part we will discuss the electromagnetic properties of wave in Metamaterial medium. So based on Maxwell equation we have:

$$\nabla \times \vec{E} = -\frac{\partial \vec{B}}{\partial t} \tag{1.1}$$

$$\nabla \times \vec{H} = \frac{\partial \vec{D}}{\partial t} \tag{1.2}$$

Where $\vec{E}$ and $\vec{H}$ are the electric and magnetic fields, respectively, and D and B are the electric and magnetic flux densities, respectively and (assuming a linear medium):

$$\vec{B} = \mu_{eff}\mu_0\vec{H} \tag{1.3}$$

$$\vec{D} = \varepsilon_{eff}\varepsilon_0\vec{E} \qquad (1.4)$$

Where ε is the electrical permittivity, ε_{eff} is the effective or relative permittivity, ε_0 is the free-space (vacuum) permittivity 8.854×10^{-12} farads/meter), μ is the magnetic permeability, μ_{eff} is the effective relative permeability, and μ_0 is the free-space (vacuum) permeability ($4\pi \times 10^{-7}$ henrys/meter). In a free of charge medium we have:

$$\nabla . \vec{D} = \rho = 0 \qquad (1.5)$$

$$\nabla . \vec{B} = 0 \qquad (1.6)$$

In a source free, isotropic, homogeneous medium:

$$\nabla \times \vec{E} = -j\omega\mu\vec{H} \qquad (1.7)$$

$$\nabla \times \vec{H} = j\omega\varepsilon\vec{E} \qquad (1.8)$$

Then we can write the wave equation as:

$$\nabla^2 . \vec{E}^2 + \omega^2\mu\varepsilon\vec{E} = 0 \qquad (1.9)$$

So the propagation constant is:

$$k = \omega\sqrt{\varepsilon\mu} \qquad (1.10)$$

In this part based on the sign of permittivity and permeability we can predict the behavior of wave in a medium where it is LHM or RHM. Especially we will deal with effective permittivity and permeability in a certain frequency band that characterized the material properties. From Equation 1.10 it seems that when $\varepsilon < 0$ and $\mu < 0$, the $\vec{E}$ and $\vec{H}$ and $\vec{k}$ vectors form a left-handed orthogonal system. By defining the energy flow which is given by Poynting vector as:

$$\vec{E} \times \vec{H} = \vec{S} \qquad (1.11)$$

It can explain the result for vector product of electric and magnetic field, so for normal condition we can find the direction of resulted perpendicular vector based on right hand. The same rule can be applied for Metamaterial but at the end the resulted vector must be reversed.
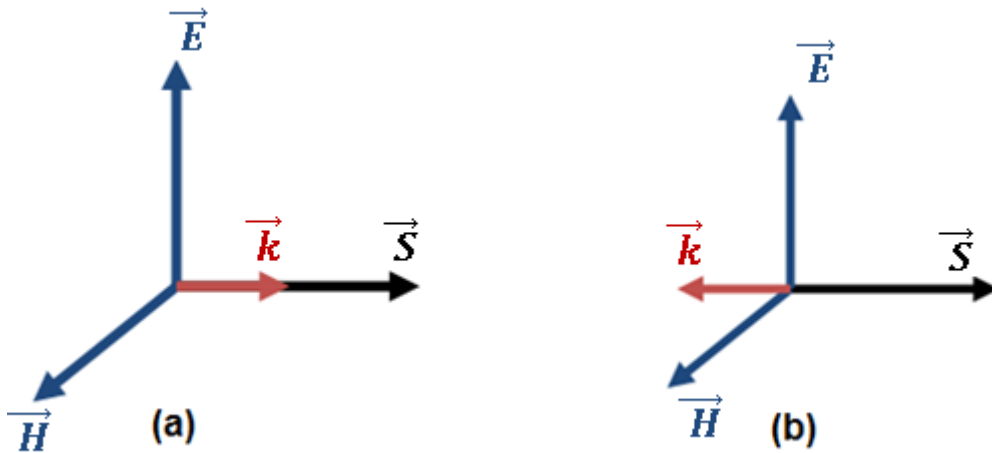
Figure 1.1. Fields vector coordinate system for (a) RHM (b) LHM.

It is obvious that if permittivity and permeability are positive the k vector will be in the same direction with $\vec{S}$ (RHM). Both negative μ and ε means that there is also propagation but in this case it is in the opposite direction of the energy density flow (LHM). The directions of $\vec{E}$, $\vec{H}$, and $\vec{k}$ for both RHM and LHM are shown in Figure 1.1. In the following we define a quadrant system to specify the sign of permittivity and permeability and the way of propagation based on the wave equation; there are four state for the sign of ε and μ.
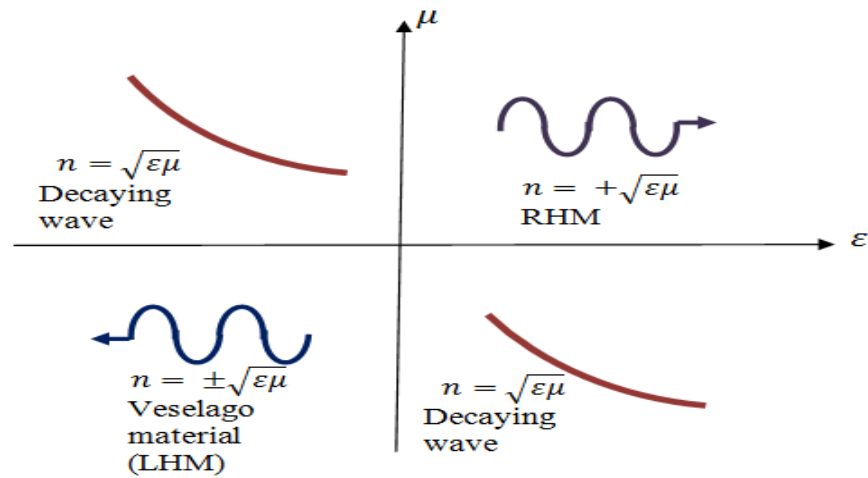
Figure 1.2. ε and μ coordinate system after [5].

In first quadrant both are in same signs and positive i.e. $\varepsilon > 0$ and $\mu > 0$. According to Equation 1.10 there will be a propagation that obeys right hand rule. All the dielectrics are such those devices. If one of those parameters is negative then the wave will not propagate so it attenuates till becomes diminished. The $\varepsilon < 0$ and $\mu > 0$ case is true for metallic materials bellow the plasma frequency and it refers to second quadrant. For $\varepsilon > 0$ and $\mu < 0$ which belongs to forth quadrant there is also attenuation. Materials such as ferromagnet and antiferromagnets near the ferromagnetic resonance behave as this. In the third quadrant which shows the Metamaterial behavior the propagation is in reverse direction of RHM because of the sign of permittivity and permeability both negative.

1.1.2. Negative Refraction

Typically the refractive index is defined by

$$n = \pm\sqrt{\varepsilon\mu} \tag{1.12}$$

Normally the positive sign is chosen for natural materials. For both negative permittivity and permeability the production is still positive but the negative sign will show the way of propagation and so wavevector. The reflection and refraction phenomena in the interfaces of two different materials with different dielectric constant are so familiar based on Snell's law which explains the relationship between angle of incidence and refraction.

Now we can study the behavior of a ray of light in the interface of a RHM and LHM. Figure 1.3 shows that based on energy flow in the interface the reflected wave is in the negative angle of whatever expected in the conventional material.
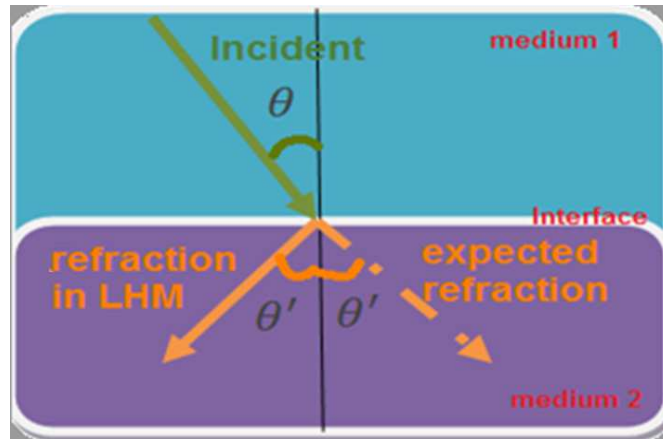
Figure 1.3. Refraction of a ray at the interface between a Right-handed medium and a left-handed medium.

As it comes from Snell's law

$$n_1 \sin \theta = n_2 \sin \theta' \qquad (1.13)$$

Where the n_1 is the refractive index of medium 1 and θ is the incident angle and the n_2 is the refractive index of medium 2 and θ' is the refractive angle. In this case the n_2 i.e. $n_2 = -\sqrt{\varepsilon \mu}$ is negative so the rays will be refracted on the same side of the normal on entering the material it means the wave propagate in negative direction.

1.1.3. Absorption Characteristics

In opaque materials the refractive index is a complex number which the real part defines the refraction and the imaginary part describes the absorption. Metamaterial constructed from opaque materials which in a certain wavelength has a negative real part of complex refractive index. Further, for definition of absorption, we need to consider the energy conservation condition given by R + T + Absorption = 1. Where R shows the reflected incident wave from structure surface, T is transmitted wave from one end point to

the other end point of structure and Absorption is the absorption amount in the structure. As most of the incident energy goes in absorption, the total scattering (R + T) of a critically coupled system must be near zero. In Chapter 3 by retrieving the effective parameters of Metamaterial we will show that in resonance frequencies by decreasing R and T simultaneously the imaginary part of refractive index will be positive so the structure shows an acceptable amount of absorption.

1.2.   Realization of LHMs

Veselago predicted that it is possible to introduce a material which has negative permeability but as it has not been find in the nature since Pendry introduce some artificial structure which couples strong magnetic field and as a result the negative permeability can be seen. Also the metallic wires below the plasma frequency can play the role of negative permittivity. So the artificial structure plus wire can give a negative refractive index medium (LHM).

1.2.1.   Negative Permittivity Medium and Negative Permeability Medium

For simple free space wave traveling the permittivity and permeability are considered constant but for Metamaterial which the permittivity and permeability are frequency dependent it is difficult to deal with them, also the Metamaterial are composite material we just put the effective values of permittivity and permeability for simulation. The lossy Drude model is used to shows the dependence of the properties of Metamaterial to frequency of coming wave. Based on lossy Drude model [5] in the frequency domain, the electrical permittivity and magnetic permeability, respectively, are described by:

$$\varepsilon = \varepsilon_0 \left(1 - \frac{\omega_p^2}{(\omega^2 + j\omega\gamma_d)}\right) \qquad (1.14)$$

$$\mu = \mu_0 \left(1 - \frac{\omega_p^2}{(\omega^2 + j\omega\gamma_d)}\right) \qquad (1.15)$$

Where ω_p is the plasma frequency, and γ_d is the damping (collision) frequency, respectively and ω is the general incoming wave frequency. As the plasma frequency is the rapid oscillation of electron density in a medium so because of a huge density of free charge in metallic materials so plasma frequency is so high. For example the plasma frequency of gold is $2\pi \times 2183\,\text{THz}$ and the damping frequency is $2\pi \times 6.46$ THz. So ω_p is the plasma frequency given blow:

$$\omega_p = \sqrt{\frac{n_e e^2}{m_e \varepsilon_0}} \tag{1.16}$$

Where n_e is the density of electrons, e is the electric charge, m_e is the effective mass of the electron, and ε_0 is the permittivity of free space. For decreasing the plasma frequency to the frequencies up to GHz regime Pendry designs an array of thin wires, this 3D structure have negative permittivity below the plasma frequency.
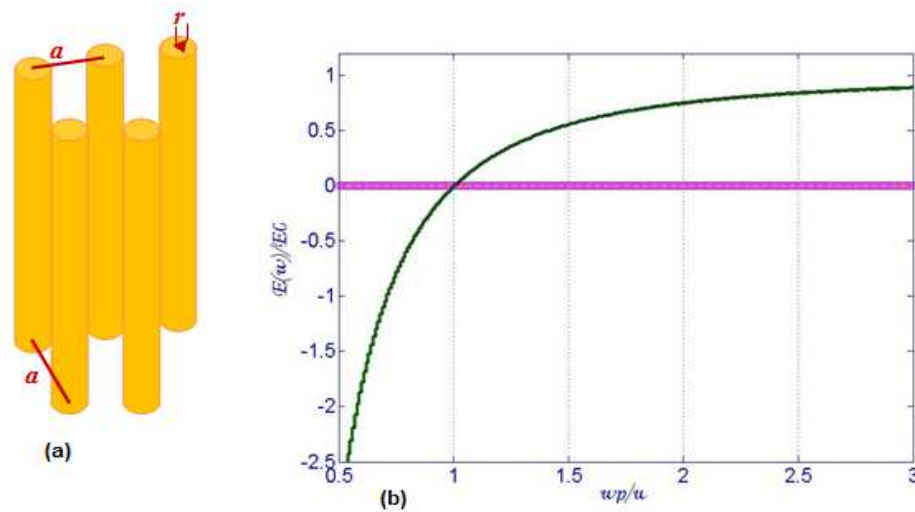
Figure 1.4. Constructing of negative permittivity medium (a) The metallic wire and (b) dependence of negative permittivity to frequency after [2].

As shown in Figure 1.4a the array of metallic wire is similar to bulk material but as they are separated thin wires with infinite longs, the effective electron density is decreased. The density is proportional to the volume of thin wires to the vacuum area. So the plasma frequency is a function of geometries of wires i.e. the radius of wires and the lattice constant. According to [2] plasma frequency of wires can be given as:

$$\omega_p = \frac{2\pi c_0^2}{a^2 \ln \left(a/r \right)} \tag{1.17}$$

The plasma frequency so the effective permittivity can be controlled by changing the dimension of wires. In Figure 1.4b the negative permittivity is achieved under the plasma frequency in such a plasma medium has been shown. As discussed earlier finding a negative permeability material is impossible in the nature. The concept of negative permeability is of particular interest, not only because this is a regime not observed in ordinary materials, but also because such a medium can be combined with a negative permittivity to form a "left-handed" material (i.e., $\vec{E} \times \vec{H}$ lies along the direction of $\vec{k}$ for propagating plane waves) [6]. Pendry proposed a split ring resonator (SRR) design [2], which can provide a narrow frequency band with negative permeability under certain polarization of incident EM wave. In Figure 1.5 the array of proposed design and the single unit cell schematic is depicted.
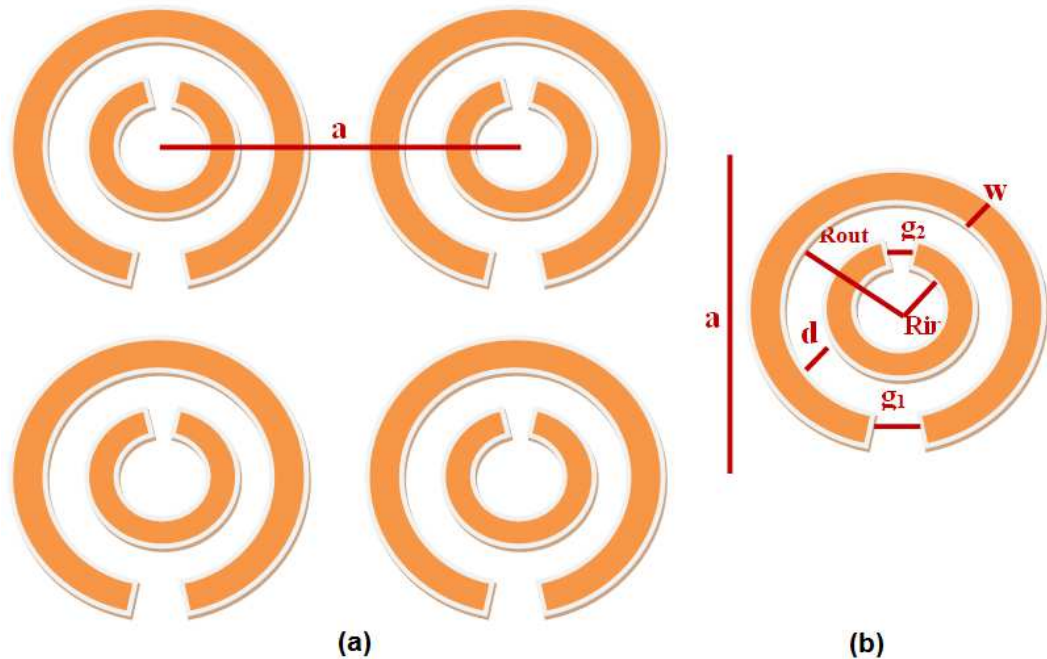
Figure 1.5. The split ring resonator (a) Array (b) Unit cell SRR with geometric parameters.

The split ring resonator is composed of two concentric circles; each has one gap with 180° phase difference. As shown in Figure 1.5b, g_1, g_2 are the gaps, R_{in} and R_{out}

define the inner and outer rings radiuses, w is the width of rings and d is the gap between two rings. In normal case the gaps and the width of rings are similar and equal. As the rings made of good conductors as gold or copper the applied magnetic field, H, can induced the circular current on the surface of the rings. Also as this structure has gaps it causes to creating a capacitor and as a length an inductor. If we consider the losses then it is a complete RLC circuit that has a certain resonance frequency. As explained in [2] the effective permeability of two concentric split rings can be written:

$$\mu_{eff}(\omega) = 1 - \frac{\omega^2 \frac{\pi r^2}{a^2}}{\omega^2 + j\omega \frac{2a\sigma}{r\mu_0} - (\omega_m)^2} \tag{1.18}$$

Where r is the radius of inner ring (R_{in}), a is the lattice constant, σ is the conductivity, c_0 and μ_0 is the speed of light and permeability in the vacuum respectively.
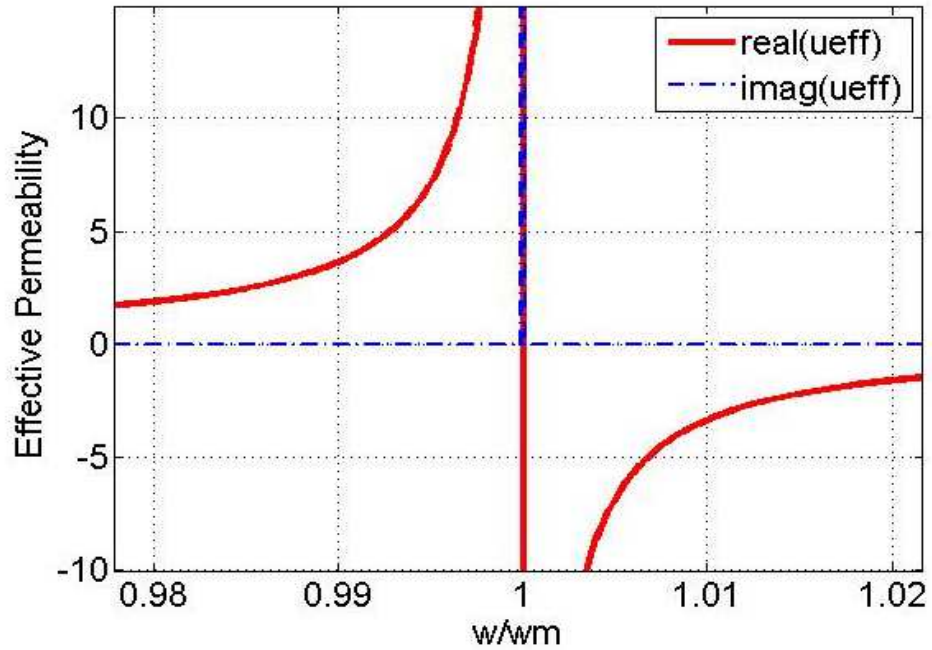
Figure 1.6. Relationship between frequency and SRR permeability.

Term $\omega_m = \frac{3ac_0^2}{\pi \ln(2w/d)r^3}$ is the resonance frequency of a structure which is a function of geometrical parameters. In Figure 1.6 we plot the permeability versus

frequency where the structure starts to show a negative permeability after resonance frequency because of coupling of magnetic field.

1.3. Basic Structure of Metamaterial

According to above discussions now we can deal with the basic structure of a Meta-material. By considering that SRR is one component of negative refractive index material so the other component is the wire. In Figure 1.7 a simple Meta-material can be seen. The square shape Meta-material first introduced by Dr. Smith and his group [6]. In this work we will work with the circular SRR in combination with wire. Whatever we expect is having negative permittivity and negative permeability simultaneously in a specified frequency band based on geometrical parameters.

Figure 1.7. Combinations of SRRs and wire as LHM.

As we will show later in Chapter 3 the stop-band of the SRR structures caused by a magnetic resonance with the negative permeability disappeared when the wires arrays were added. Instead, a pass-band existed, where the effective permittivity and the effective permeability are both negative.

1.4. Literature Review

After introducing of first SRR in 2000 [2] there have been a great effort to bring the resonance frequency of SRR from microwave to optical frequency. So by sizing and scaling down of the structure from millimeter rang to hundreds of nanometers, researchers from different groups have successfully fabricated and demonstrated the magnetic response of SRR structures operating at 1 THz [7], 2 THz [8], 100 THz [9], and 200 THz [10]. The scaling has a reciprocal relation with frequency which is true up to several THz. Because of the breakdown of the linear scaling, it is more difficult to increase the resonance frequencies after that limit. Thus, researchers must look for alternative designs suitable for THz and optical regimes. The short wire pair designs were realized and published independently by two different groups in 2005 [11 - 13]. These designs show that pairs of metallic wires, separated by a dielectric spacer, can provide magnetic resonance and negative [5]. In addition, the short wires also support electric resonance with negative permittivity, which results from the parallel current in the wires. Although short wire pairs can provide both the magnetic resonance and the electric resonance, overlapping these resonances is very difficult [14]. In order to obtain a left-handed material, additional structures providing negative permittivity are needed. One method is to introduce extra continuous wires next to the pairs [13], and another method is to change the shape of the wires. A fishnet structure was introduced [15,16], realizing both $\varepsilon < 0$ and $\mu < 0$ at infrared frequencies and later on in the optical [17]. The fishnet structure was considered as the best LHM design in the optical regime, and a few variants of fishnet structures were studied in [18,19]. The summery is brought in Figure 1.8.
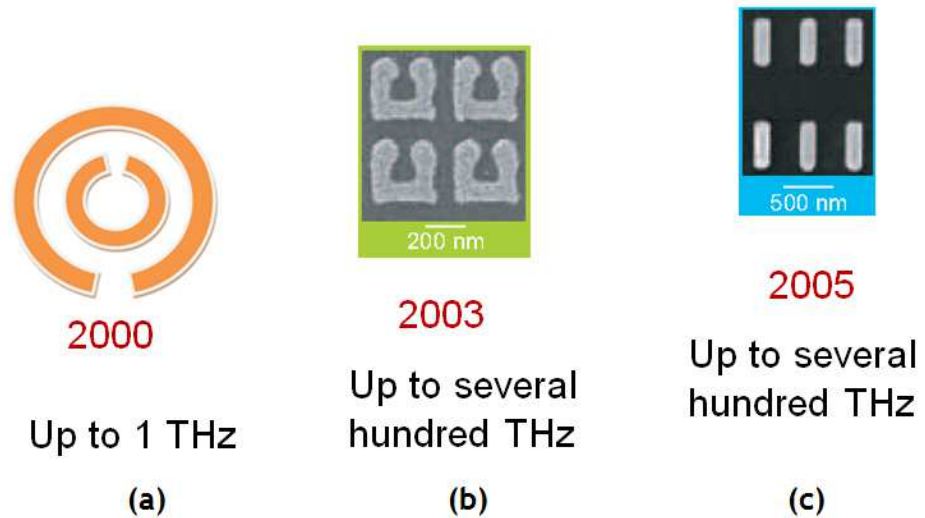
Figure 1.8 The progress in the negative permeability and negative index materials. (a) Circle SRR [2] (b) U-shaped [5] (c) Pairs of metallic short-wire pair [11-13] after Copyright (2007) AAAS.

1.5. Terahertz Imaging

Based on a report of Technology Review (MIT) 2004 THz technology is selected as one of 10 emerging technologies that will change world. Tera hertz waves are working between 0.1 THz and 10 THz frequency band so the wavelength of 3mm -30μm. their energy can vary between 0.41 and 41 meV. As their energy has minimum harmful effects on sample on the test it is going to get more interest for medicine imaging purposes. In addition many materials exhibit characteristic spectral features in the THz frequency range (particularly >1 THz), enabling THz spectroscopy to be used as a tool to uniquely identify chemical species. Figure 1.9 shows the absorption frequency band of some drugs and common explosives. It seems that the Cocaine as a common drug-of-abuse has a high amount of incident wave absorption near 4 THz. Also other derived material has somehow same characteristics. Figure 1.9b depicts the absorption characteristics of two different types of explosives in THz frequency band.
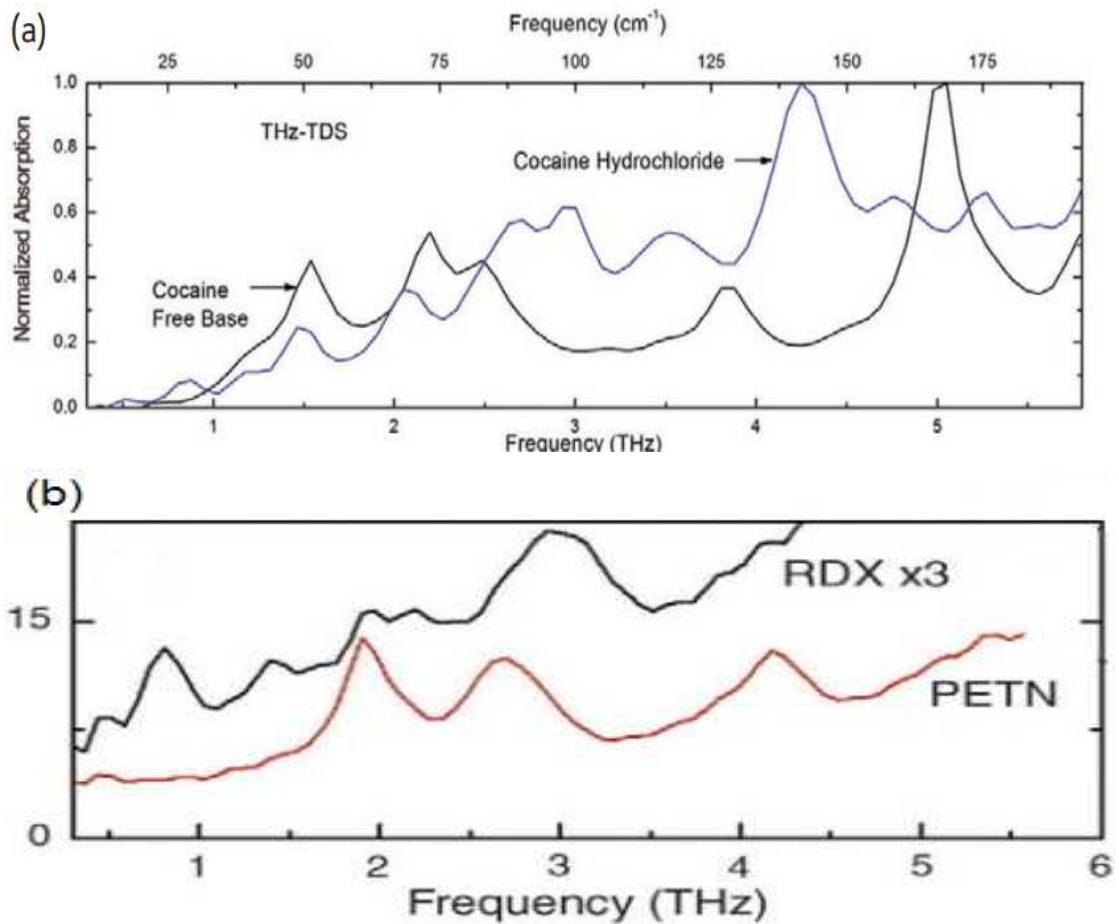
Figure 1.9. THz absorption spectra of (a) Cocaine and (b) Pure explosive samples (PETN and RDX) [20].

There are rich potential applications of the terahertz radiation:

(i)   Medical imaging: Terahertz radiation is able to penetrate up to several millimeters into some tissues with low water content. Its sensitivity to the water content makes it a promising probe of some type of cancers. Unlike X-rays, terahertz radiation is non-ionizing: its energy is too low to cause any damage to the tissue. Terahertz image of a skin by Teraview's medical-imaging equipment is shown in Figure 1.10.
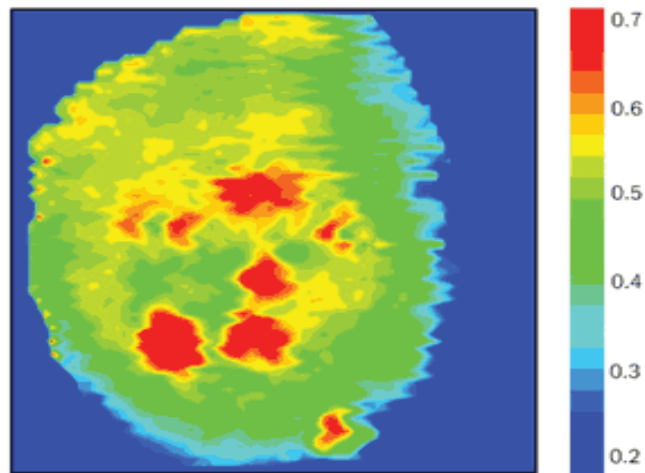
Figure 1.10. Terahertz image of a part of a patient skin. The dense regions show the cancerous cells [21].

It offers the ability to produce 3D images at high resolution through thick tissue using molecular markers, such as water, to provide spectral and absorption information to differentiate between cancerous and non-cancerous tissues, non-invasively and using non-ionizing radiation [21].

(ii) Security imaging: Terahertz radiation sees different things as compared to visible light. Notably, terahertz radiation passes through majority of plastics and clothes, but it does not penetrate through water. This makes the terahertz radiation an interesting tool for security checks.

Figure 1.11. Illustration of concealed object by ThruVision TS4 [22].

This instrument employs a passive approach means it just interpreted the receiving Terahertz radiation emitted from individuals and their environments. The brighter region in Figure 1.11 is a concealed object made from metal.

(iii)   Telecommunications: Systems based on waves with terahertz carrier frequencies can support a broadband modulation, and thus achieve very high transmission rates (principally of the order of 10^{11} bits·s^{-1}).

2. SPLIT-RING RESONATORS

If we consider the Split Ring Resonator as most important part of the LHM which mostly deals with magnetic response of it, in this chapter we will explain the characteristics of proposed SRR under EM wave. It is important to predict the respond of structure under different polarization. After that the analytical model can prove that prediction so a simplified model based on lumped parameters can be useful. At the end the proposed design, analytical approach and simulation result will be provided to make the comparison.

2.1. Concept and SRR's Role in Optical Regime

There are different types of ring resonators especially who have splits. Also the shapes of structures can be squares or circles or other geometries. But all of them are common in having the gaps. Also the number of gapes can vary. The importing thing is we need a surface for conducting current so component must be made out of nonmagnetic metal such as copper. This electrical element defines capacitances and inductances that describe resonance frequencies. So controlling the resonance frequency seems to be simple. As all the lumped elements are functions of dimensions and sizes of structures for increasing the resonance frequency scaling the dimension is enough. Consider:

$$f = \frac{1}{2\pi\sqrt{LC}} \tag{2.1}$$

$$L = K_1 \frac{A}{l} \tag{2.2}$$

$$C = K_2 \frac{A}{g} \tag{2.3}$$

$$A = w \times t \tag{2.4}$$

Where f is the resonance frequency, L and C are the gap capacitance and self inductance of ring, K_1 and K_2 are the constants related to physical properties of materials, A is the cross section, l is the effective length and the t is the thickness of ring. With considering the above mentioned formulas we can conclude:

$$f \propto \frac{1}{2\pi\sqrt{a^2}} \qquad (2.5)$$

Where a is the lattice constant. Note that a is also the scaling factor for all the aforementioned geometrical parameters.
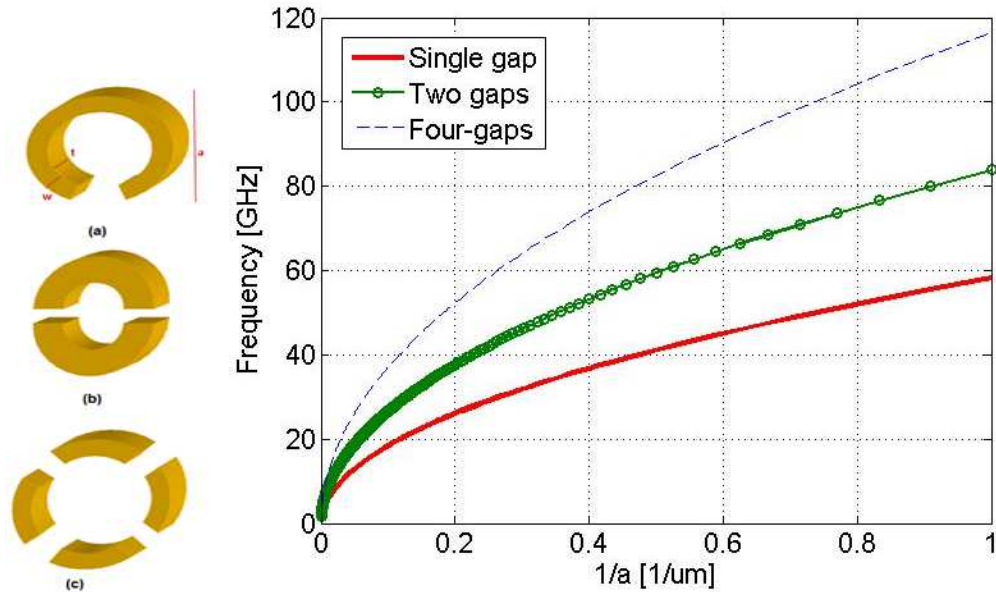
Figure 2.1. Schematic of single ring resonators with (a) Single gap, (b) Two gaps, (c) Four gaps.(d) Dependency of resonance frequency to the scaling factor of a (unit cell dimension) after [5].

It is obviously from Figure 2.1 can be seen that the scaling method is useful just up to 20 THz for ring that just have one split. After this range the dependency of frequency to the geometrical parameters is not linear also after a certain size there is no significant change so called saturation of resonance frequency. For reaching the higher frequency up to optical frequencies it seems that we need other shapes of ring resonators or also other types of materials. Here the suggestion is increasing the number of splits. Consider the magnetic excitation (discussed in Section 2.2.2), which the magnetic field is out of plane

and electric field is perpendicular to the gap, and taking into account just the capacitors that gaps contribute, so more numbers of gaps mean more series capacitors and less overall capacitance results in higher frequencies (Figure 2.1d). Also saturation is repeating in higher frequencies (more than 120 THz), bringing proper material especially for dielectric substrate is important for optical frequencies. In all studies we consider a dielectric constant for every frequency despite it is more dependent in high frequencies.

2.2.   Electric and Magnetic Response of SRRs

In this section we will deal with the response of SRR to the different types of excitation. It will be very useful to predict this response under different orientation of magnetic and electric field, observing them also can be a necessary clue in future works. For the first step we do all the experiments with HFSS simulator. In the following an introduction will be discussed the full wave electromagnetic solvers i.e. Ansoft's HFSS then the simulated results for all possible excitation are plotted.

2.2.1. Use a FDTD Tool for Simulation

Among all commercial full wave electromagnetic solvers such as Ansoft's HFSS or CST Microwave Studio, we chose the HFSS which is based on finite elements method (FEM), is used for the analysis of SRR structures in this work.

The important point in using of HFSS is defining the boundary condition. In order to get the transmission or reflection spectrum we need to extract scattering parameters using HFSS which considers the sample in confront with a plane wave excitation. Constructing frequency independent layers for time varying magnetic and electric fields are necessary. To simulate the behavior of a single SRR unit cell in isolation, these types of layers named "perfectly matched layer (PML)" [23] must be implemented. For the electric filed a PEC (Perfect Electric Conductor) and for magnetic vector a PMC (Perfect Magnetic Conductor) are defined as PMLs. The place and distances of these layers are so important for computing the complex S-parameters. In Figure 2.2 a sample under simulation condition as shown. The position of PEC, PMC and ports are shown.
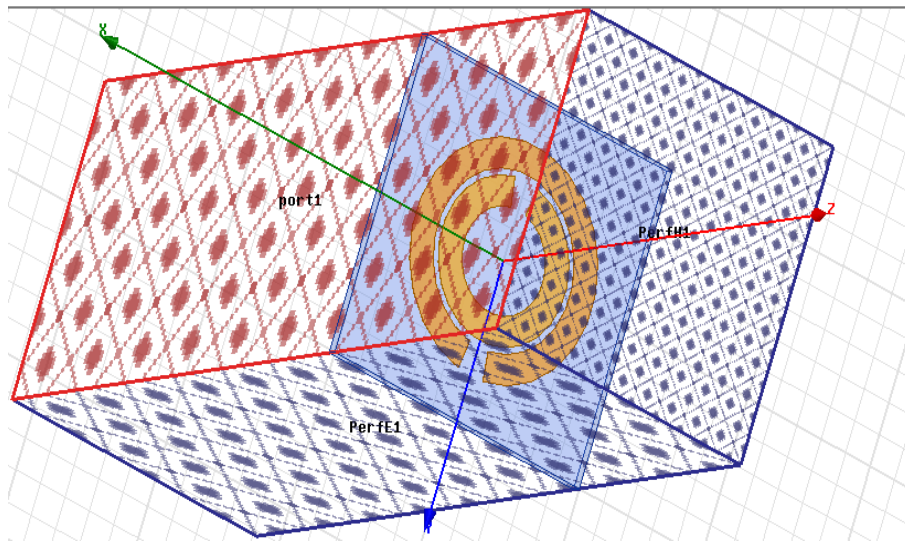
Figure 2.2. Boundary condition in HFSS simulator. PEC, PMC and Port.

By considering a vacuum cubic surrounded the sample, surfaces of this cubic used for definition of PMLs. The electric filed is along the gap and time varying magnetic field is perpendicular to the lane of structure (see Figure.2.2). We need to define a source and receiving ports as it is shown (port 1, second port is not shown in figure).

2.2.2. EM Response of SRRs in Different Polarizations

The fact that the electrons in a conductive medium such metallic part of SRR can have different responses to the different arrangement of the EM incident wave, forces us to study possible types of excitation. The configuration of incident electric and magnetic field and propagation vector can defines three possible excitations. In this part for simplicity we simulated a single ring resonator with dimension of r = 26µm, w = 7µm, g = 2µm and thickness of 0.5µm made of copper. The ring is structured on top of 85*85 μm^2 substrate made of Arlon AD350A (tm), dielectric constant = 3.5 and dielectric loss tangent = 0.003. The simulated under three different configurations are as shown in Figure 2.3.
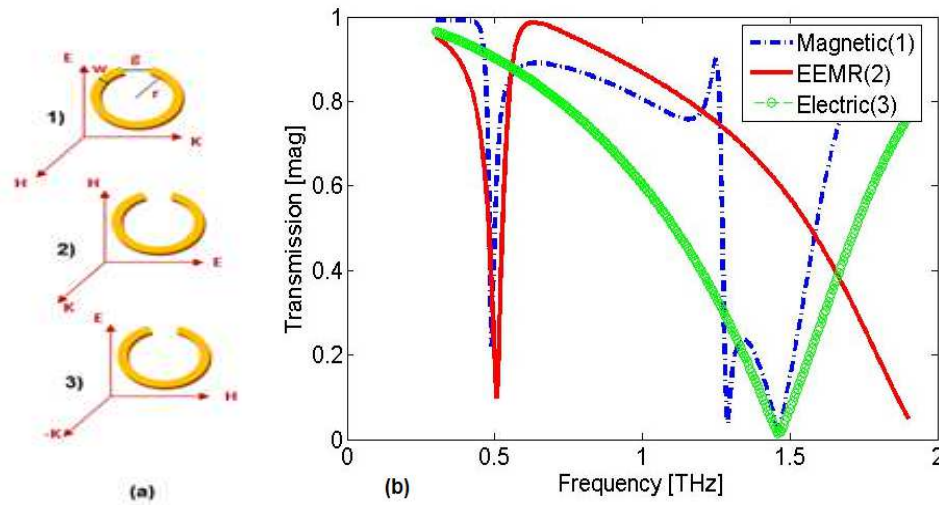
Figure 2.3. Excitation of SRRs (a) Three different configurations of incident electric field, $\vec{E}$, magnetic field, $\vec{H}$, and wave vector, $\vec{k}$, (b) Transmission spectra for three different excitations, Magnetic (blue-dash), EEMR (Red- line) and Electric (Green- circle) after [5].

First configuration known as magnetic excitation as the propagation is along the gap and magnetic field causes to induce a surface circular current on SRR. Hence one could conclude that this magnetic resonance appears only if the external magnetic field H is perpendicular to the SRR plane [3]. This current can induce another magnetic field which is anti-parallel to the incident $\vec{H}$ field. This causes a negative permeability so magnetic resonance in near 0.5 THz (Figure 2.3a.1). As shown in Figure 2.3a.2 $\vec{k}$ perpendicular to the SRR plane and $\vec{E}$ parallel to the bottom part of SRR also excites a magnetic resonance at ω_m [3], [24 - 27]. Electric field is along the gap so the electric charges contribute gap capacitor forces circular current induced by $\vec{E}$ field so second resonance frequency almost is similar to the magnetic resonance, called Electric Excitation coupled with Magnetic resonance (EEMR). Third one called electric resonance and takes place at higher frequencies because of contribution of just electric field. The $\vec{E}$ field divides the ring into two electrically separated parts posing an electric dipole moment which brings purely electric response at 1.45 THz. Figure 2.3b shows the transmission spectra for these different types of excitation.

2.3. Modeling

In one hand the SRR is built from a high conductive material that perpendicular $\vec{E}$ and $\vec{H}$ fields with together can induced current on its surface that flow in closed loops, in the other hand Lumped electrical elements in contribution with the charges induced by magnetic field make an RLC resonance circuit. In the following the modeled SRR by equivalent circuit based on lumped Resistor, Capacitor and Inductor is advantageous to predict the magnetic behavior of SRR. Also the retrieved effective permittivity and permeability will be done.

2.3.1. Basics of SRR Modeling by Equivalent Lumped Parameters

At first glance the shapes of double SRR particle was introduced by Pendry *et al*. (1999) seem to be a wise choice to reduce the resonance frequency to the desired frequency by adding the second ring as increasing the capacitive load. Indeed, these two loops have two distinct resonance frequencies because both of them represent a capacitance and inductor. But we must consider the role of second ring in coupling fact. The common magnetic flux is interpreted as a mutual capacitance between loops. The structure will have two resonance responses but the first one with larger magnetic response will be taken into account for designs. The schematic of double SRR and the contribution of all capacitances are shown in Figure 2.4. For inductance part we consider rings as conductive strips with certain length.
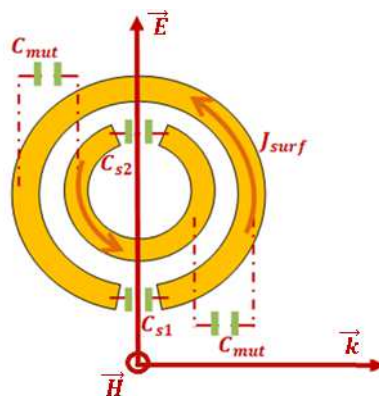
Figure 2.4. Unit cell geometry for SRR with contribution of capacitors and distribution of currents (arrows).

This model is introduced [28], [29] based on magnetic excitation so the electric field makes SRR as a dipole with negative and positive charge distribution around gaps. The magnetic field is perpendicular to the surface of SRR and induced a circular current as it is shown in Figure 2.4 (arrows). In the following we will explain the capacitors also inductors and resistors. Firstly for the mutual capacitance based on [29] an approximate relation of the broken loops in the SRR particle:

$$C_{mut} = 2b\varepsilon_{eff}\varepsilon_0 \cosh^{-1}(\frac{2w}{d}) \tag{2.6}$$

Which ε_{eff} is the effective permittivity refers to the effect of the width and height of a micro strip on ε and d is the gap between rings and:

$$b = \frac{(R_{in} + R_{out} + w)}{2} \tag{2.7}$$

It is obvious that this capacitance built up in gaps between rings. The second contribution to the capacitance is due to charges on the surface of the ring [30].

$$C_{surf} = \int_{\theta}^{\pi} \frac{\sigma R d\theta}{V} = \varepsilon_0 h\theta \int_{\theta}^{\pi} \frac{cot(\theta/2)}{\pi - \theta} d\theta = \frac{2\varepsilon_0 t}{\pi} ln\frac{4R_/}{g} \tag{2.8}$$

The surface capacitor calculated for each ring so $R_/$ is once R_{in} and for outer ring is R_{out}. The third contribution to the capacitance is due to charges in the gap. The gap can be seen as a parallel plate capacitor [30]:

$$C_{gap} = \varepsilon_0[\frac{wt}{g} + \frac{2\pi t}{ln\ (2.4t/w)}] \tag{2.9}$$

Now we can write an expression for overall capacitance. The mutual capacitances are series with together and in parallel with the others so:

$$C_{overall} = C_{gap} + C_{surf} + \frac{C_{mut}}{2} \qquad (2.10)$$

Inductance can be approximated by that of the closed ring [29].

$$L = \mu_0 R_/[log\left(\frac{8R_/}{r_0}\right) - 2] \qquad (2.11)$$

and

$$r_0 = \frac{w}{4} \qquad (2.12)$$

For two concentric loops whose radii do not differ much the following approximation for the mutual inductance can be drawn [29]:

$$M = \mu_0 a_{1,2}[(1 - \xi)\, ln\left(\frac{4}{\xi}\right) - 2 + \xi] \qquad (2.13)$$

and

$$a_{1,2} = R_{in,out} + \frac{w}{2} \qquad (2.14)$$

where $\xi = \dfrac{(a_1 - a_2)}{2a_1}$ is a small parameter ($\xi < 0.25$).

And the resonance frequency [29]:

$$\omega_m^2 = \frac{1}{\sqrt{C_1 C_2 (L_1 L_2 - M^2)}} \qquad (2.15)$$

Which C_1, C_2 and L_1, L_2 are lumped capacitances and inductances for inner and outer rings respectively. M is mutual inductance. For losses part we consider two types of resistances. First R_c relates to conductor losses and the second term is R_d because of dielectric losses.

$$R_c = \frac{2\pi R_/ - g}{\sigma \delta 2(w + t)} \tag{2.16}$$

$2\pi R_/ - g$ is the effective length of SRR, σ is the conductivity of metal, δ is skin depth in metal, w is width of the metal stripes and t is the thickness of metal layer. While modeling the conductor losses by R_c, good conductor assumption has been made. For good conductors, skin depth δ is given as

$$\delta = \frac{1}{\sqrt{\pi f \mu \sigma}} \tag{2.17}$$

In the expression of R_d, on the other hand:

$$R_d = \frac{g}{wh\omega\varepsilon \tan \alpha} \tag{2.18}$$

$\tan \alpha$ is the loss tangent of the substrate. As defined earlier, w is the width of metal strip and h is the thickness of substrate and $\omega = 2\pi f$.

2.3.2. Modeling of a SRR Unit Cell by an Equivalent RLC Circuit

Among all literature all wanted to model their structure with a good RLC resonator model which mathematically can prove the working frequency band of proposed structure before fabrication. The scattering parameters are well suited tools to study the transmission also reflection spectra. They can explain the behavior of a two port circuit in high frequencies. In this part a series RLC circuit in shunt branch is studied. Each ring has a defined value of R, C and L which correspond to their geometrical properties. Also because of coupling factor we have to consider the role of a mutual inductor in between.
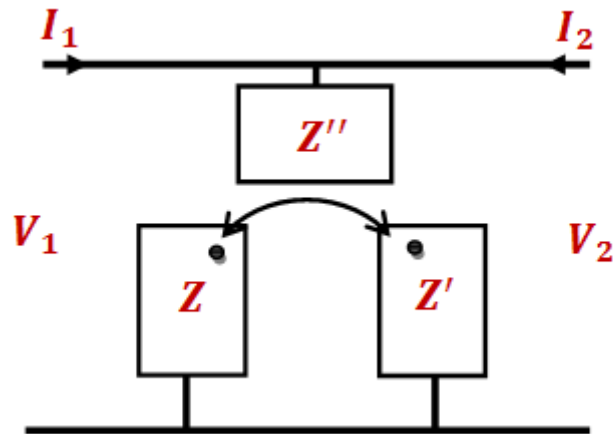
Figure 2.5. Two-port equivalent circuit representation of a double loop SRR cell with RLC resonant circuit in the shunt branch.

Where Z and Z′ represents the impedances of rings and Z″ is the mutual inductor. The equivalent Pi model of the proposed circuit is shown in Figure 2.6.
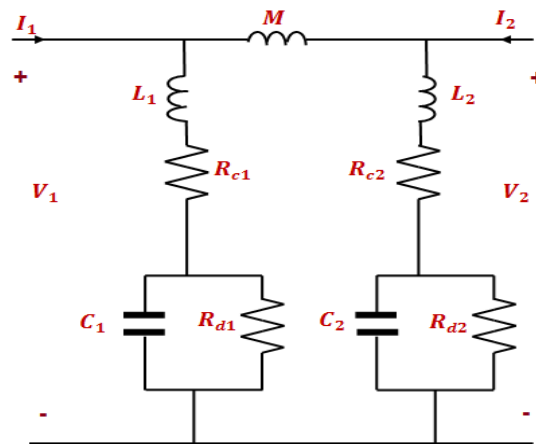
Figure 2.6. Pi model of DSRR under magnetic excitation based on lumped RLC parameters.

The impedance matrix of equivalent circuit can be written as:

$$Z = \begin{bmatrix} Z_{11} & Z_{12} \\ Z_{21} & Z_{22} \end{bmatrix}$$

(2.19)

As the circuit is symmetric so $Z_{11} = Z_{22}$ and $Z_{21} = Z_{12}$ then:

$$Z_{11} = \frac{V_1}{I_1} , I_2 = 0 \tag{2.20}$$

so:

$$Z_{11} = \frac{(A_1 + A_2) \times (B_1 + B_2)}{(1 + C_1 R_{d1} s) \times (A_1 + A_2) + (1 + C_2 R_{d2} s) \times (B_1 + B_2)} \tag{2.21}$$

where

$$A_1 = R_{d2}(1 + C_2 R_{c2} s + L_2 C_2 s^2 + M_2 C_2 s^2) \tag{2.22}$$

$$A_2 = Ms + R_{c2} + L_2 s \tag{2.23}$$

$$B_1 = R_{d1}(1 + C_1 R_{c1} s + L_1 C_1 s^2) \tag{2.24}$$

$$B_2 = R_{c1} + L_1 s \tag{2.25}$$

$$s = j * \omega \tag{2.26}$$

and

$$Z_{12} = \frac{V_1}{I_2} , I_1 = 0 \tag{2.27}$$

so:

$$Z_{12} = \frac{q_1 q_2}{q_1 + Ms + q_2} \tag{2.28}$$

where

$$P_1 = \frac{R_{d1}}{1 + R_{d1} C_1 s} \tag{2.29}$$

$$P_2 = \frac{R_{d2}}{1 + R_{d2}C_2 s} \tag{2.30}$$

$$q_1 = L_1 s + R_{c1} + P_1 \tag{2.31}$$

$$q_2 = L_2 s + R_{c2} + P_2 \tag{2.32}$$

It is also possible to obtain the scattering parameters of a given two-port network from its Z-parameters as summarized below [31]:

$$S_{11} = \frac{(Z_{11} - Z_0)(Z_{22} + Z_0) - Z_{12}Z_{21}}{(Z_{11} + Z_0)(Z_{22} + Z_0) - Z_{12}Z_{21}} \tag{2.33}$$

$$S_{11} = S_{22} \tag{2.34}$$

$$S_{12=} \frac{2(Z_{11}Z_0)}{(Z_{11} + Z_0)(Z_{22} + Z_0) - Z_{12}Z_{21}} \tag{2.35}$$

$$S_{12} = S_{21} \tag{2.36}$$

2.4. Design of Split Ring Resonator

With that introduction we can go over the proposed design. For the beginning four different designs will be introduced. All the dimensions are gathered in the Table 2.1. In this part we calculated the expected resonance frequency based on Equation 2.6 to Equation 2.36.

Table 2.1. Dimension of proposed design.

Design	1	2	3	4
R_{out} (mm)	2.6	3	3.6	4
w (mm)	0.9	0.9	0.9	0.9
R_{in} (mm)	1.5	1.9	2.5	2.9
g (mm)	0.2	0.2	0.2	0.2
t(μm)	14	14	14	14
FR4 thick (μm)	130	130	130	130

The structure is a double SRR made of copper on a FR4 substrate. Four different sizes of radius show four different resonance frequencies so extended experiences. In all designs the thickness of FR4 layer and metallic strip are constant. Also the split and the gap between rings are similar and 0.2mm. The unit cell size is $9 \times 9 mm^2$ for all sizes. Constructing a excel sheet contains all the information about analytical calculation bring us the following table showing the predicted resonance frequencies.

Table 2.2. Results of analytical model for four different ring dimensions.

Design	1	2	3	4
f (GHz)	6.22	4.73	3.49	2.97

As we expect because of capacitive also inductive load added to the ring by increasing the dimension of rings so bigger the SRRs geometries, smaller the resonance frequency. The plotted transmission spectrum for each design based on analytical model is presented in Figure 2.7 to Figure 2.10 together with simulation results.

Figure 2.7. Plotted Transmission spectrum for Number 4 design (4 mm radii) Red-line shows the extracted curve from analytical model and blue-dash is the HFSS result.

Based on simulation result for the biggest structure the resonance frequency will be at 3.7 GHz. The model depicted the resonance dip at 3.25 GHz. Also we need to consider that the model based on a second order model which may have another dip/s in off resonance band. 14% error can be seen as Figure 2.7.

Figure 2.8. Plotted Transmission spectrum for Number 3 design (3.6 mm radii) Red-line shows the extracted curve from analytical model and blue-dash is the HFSS result.

For design number three, as the dimensions gathered in Table 2.1 simulation tool predicts resonance frequency will be at 4.3 GHz. The model depicted the resonance dip at 3.87 GHz. In the Figure 2.8 another resonance can be seen far from the expected resonance. As mentioned before second order equivalent circuit would show other resonances if the lumped parameters have very different values. 10% variation achieved.
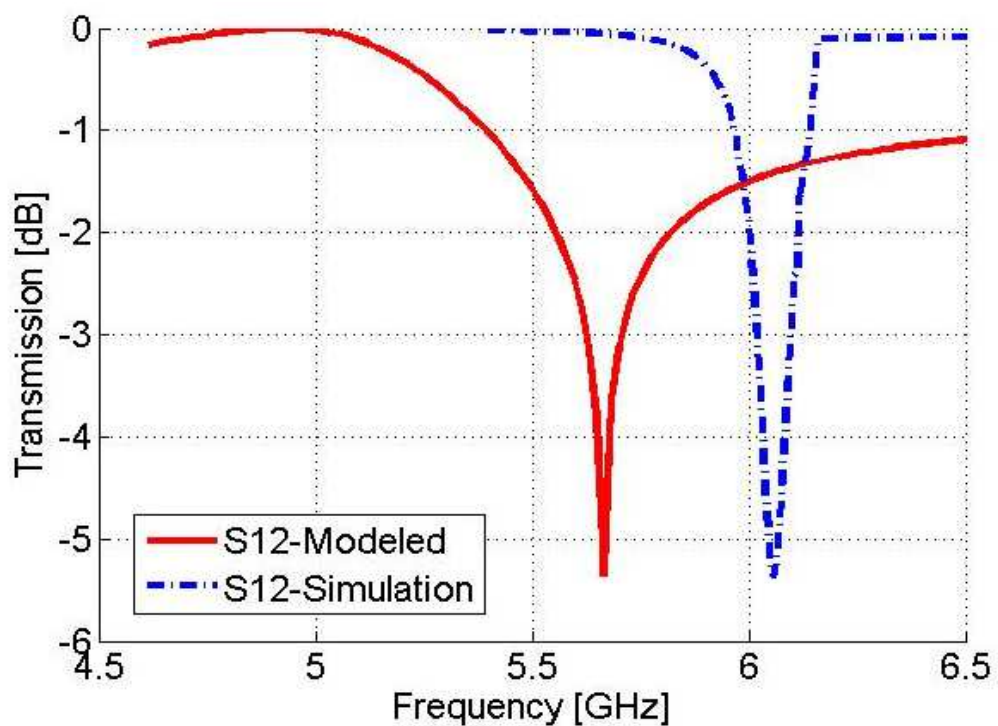
Figure 2.9. Plotted Transmission spectrum for Number 2 design (3 mm radii) Red-line shows the extracted curve from analytical model and blue-dash is the HFSS result.

For design number two, as the dimensions gathered in third row of Table 2.1 simulation tool predicts resonance frequency will be at 6.1 GHz. The model depicted the resonance dip at 5.6 GHz. In the Figure 2.9, 8% of validation error can be seen.
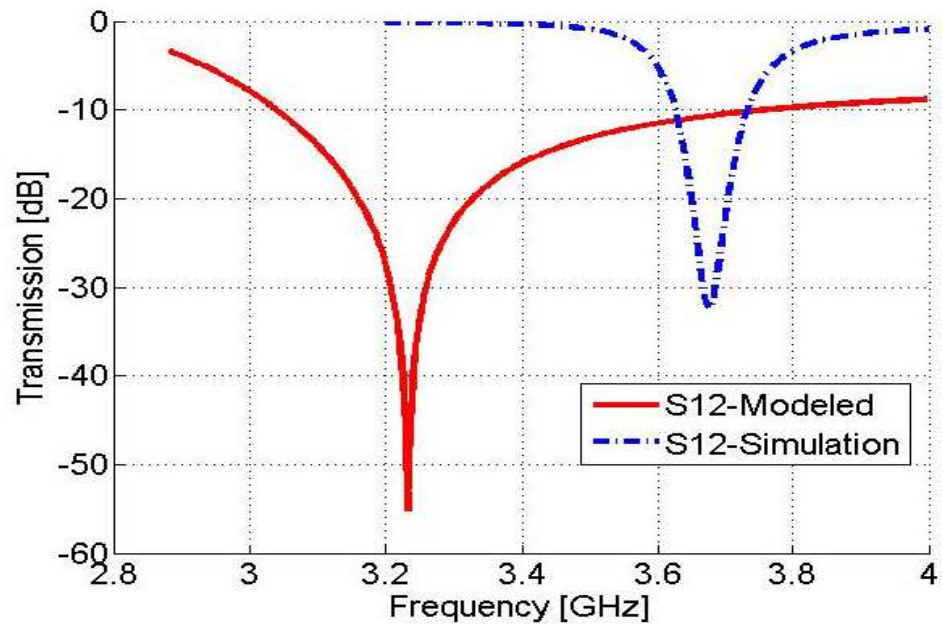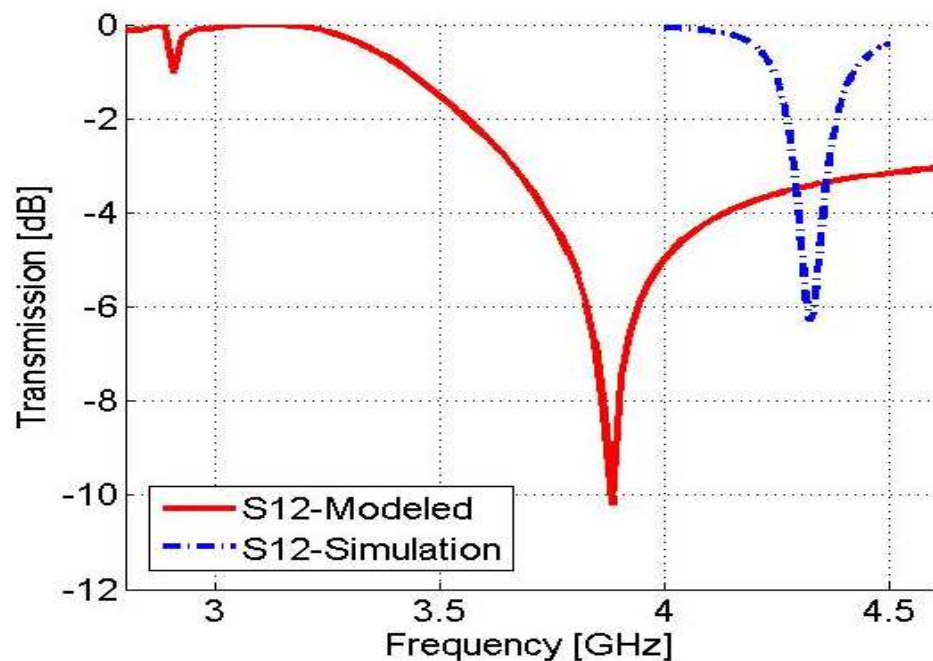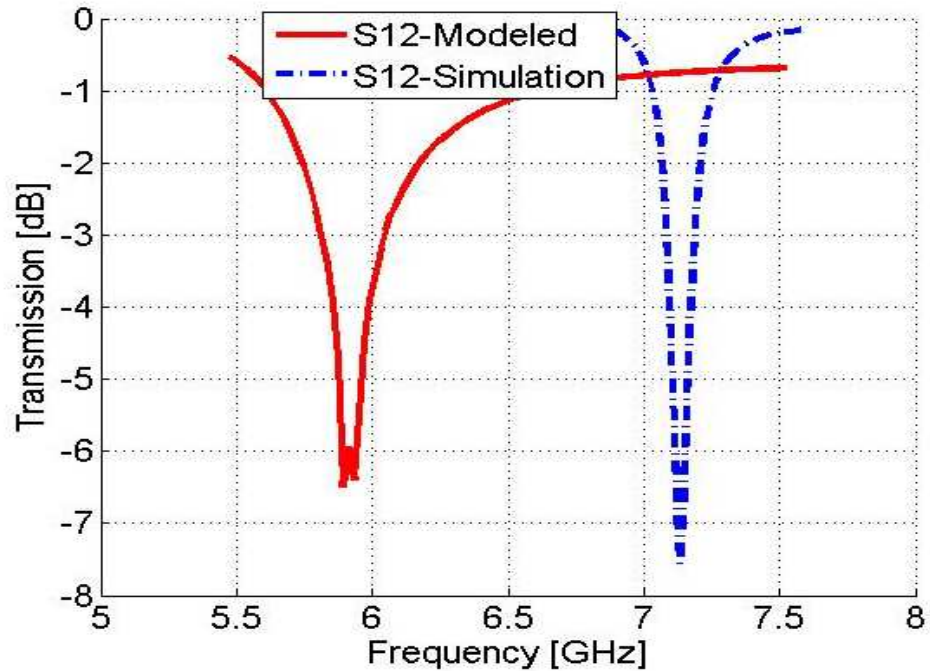
Figure 2.10. Plotted Transmission spectrum for Number 1 design (2.6 mm radii) Red-line shows the extracted curve from analytical model and blue-dash is the HFSS result.

In comparison between simulation curves and modeled one for smallest design we can see that there is a mismatch of 16 % as the simulated resonance is in 7.1 GHz and the resonance frequency of analytical model comes in 5.9 GHz. I need to explain that because of a big variation in values of inductances for inner and outer rings for number one design, there were three different dips which were out of required frequency band so an amount of error factor is considered then equivalent model result is plotted for new values. Also we need to consider that the frequencies we brought in Table 2.2 are just a certain resonance frequency which comes from Equation 2.15. The modeled plots consider a certain capacitances and inductors despite the FDTD simulation may consider the effects of other parameters. Whatever is presented here is just a method to predict the behavior of SRR.

3. LHM BASED ON SPLIT RING RESONATORS

Recently, periodically arranged metallic thin wires and Split Ring Resonator (SRRs) structures have attracted much attention in the scientific community. In left-handed materials, negative permittivity and negative permeability are realized separately by wire arrays and SRR arrays, respectively. As they provide negative permittivity and negative permeability medium so the electromagnetic wave cannot propagate in this region thus a gap will be seen at transmission frequency band. In this chapter based on the facts discussed earlier the behavior of Meta-material will be studied. The transmission and reflection spectrums so the retrieved permittivity and permeability can give us useful information about the absorption of proposed design.

3.1. Operation of the SRR and Wire

The idea of simultaneous negative permittivity and permeability was introduced by Veselago which predicted that via artificially constructed materials, along with simultaneously negative ε and μ, can all be overcome. However, obtaining a simultaneously negative ε and μ and, therefore, a negative index of refraction is a significant challenge. As discussed in Chapter 1 by assembling thin metallic wire structures into a periodic medium with appropriate parameters, negative permittivity can easily be achieved at microwave frequencies. Metallic thin wires arranged periodically are good candidates for a negative ε medium, because this structure exhibits a plasma frequency below which the material is opaque [32]. In 1999, Pendry *et al.* introduced several configurations of conducting scattering elements displaying a magnetic response to an applied EM field when grouped into an interacting periodic array [32]. The resonant behavior of SRRs is due to the capacitive elements (gaps and splits), which in turn results in rather high positive and negative values of permeability near the magnetic resonance frequency. It has been shown that the effective plasma frequency, in the composite materials is substantially lower than the plasma frequency of the wires [5].

3.2.   The Transmission and Reflection Response

Transmission spectrum (S12) of the Meta-material unit cell is obtained by HFSS using both PML and PEC type boundary conditions. The isolated unit cell structure is analyzed when PML boundaries are used. The amount of reflected wave from structure surface will be measured (S11) as reflecting coefficient.

3.2.1.   The Retrieved Parameters

There is a need to calculate the effective parameters explicitly. In order to obtain the effective electromagnetic parameters of LHM, i.e., the effective permittivity and the effective permeability, Smith *et al.* proposed a retrieval procedure. The idea was to model the Meta-material as an isotropic homogeneous slab, and calculate the effective parameters of the homogenous slab, from the measured or simulated meta-material transmission, T, and the reflection, R, by using the theoretical formulas for the slab. The resonance behavior of the retrieved permeability and the negativity of the retrieved Permittivity were observed for the composite structure consisting of wire and SRR. The relationship between transmission coefficient for wave incident normally to the face of a 1-D slab in vacuum with length of *a* and the refractive index is [33]:

$$T^{-1} = \left[\cos(nka) - \frac{i}{2}\left(Z + \frac{1}{Z}\right)\sin(nka)\right]e^{ika} \qquad (3.1)$$

Also the reflection coefficient related to Z and n by:

$$\frac{R}{T'} = -\frac{1}{2}i\left(Z - \frac{1}{Z}\right)\sin(nka) \qquad (3.2)$$

And

$$\mathrm{T'} = \mathrm{e}^{ika}\mathrm{T} \qquad (3.3)$$

Where $k = \frac{\omega}{c}$ is the wave vector in vacuum. Equation 3.1 and Equation 3.2 can be inverted to calculate n and z from t and r. By completing this inversion, we obtain:

$$Z = \pm \sqrt{\frac{(1 + R)^2 - T'^2}{(1 - R)^2 - T'^2}} \qquad (3.4)$$

Although Equation 3.4 has a relatively simple form, both are complex functions with multiple branches, which lead to ambiguities to determine the final expression of ε and μ. We need additional information about material properties to fix these ambiguities. For passive materials the real part of the impedance is positive so Re $(Z) > 0$, which determine the sign in Equation 3.4. Similarly, the requirement for the imaginary part of the refractive index, Imag $(n) > 0$, for the passive material, shows the sign of n:

$$Im(n) = \pm\, Im\left(\frac{\cos^{-1}(\frac{1}{2T'}[1 - R^2 - T'^2])}{ka}\right) \qquad (3.5)$$

After solving the right hand side of Equation 3.5 we can decide on which one of its root can give us the positive value. However Re (n) is complicated by the branches of the arccosine function:

$$Re(n) = \pm\, Re\left(\frac{\cos^{-1}(\frac{1}{2T'}[1 - R^2 - T'^2])}{ka}\right) + \frac{2\pi m}{ka} \qquad (3.6)$$

Where m is an integer. Equation 3.6 shows the branches can be very close to each other when a is large, which makes the selection of the correct branch difficult in the case of dispersive medium. So we should take the smallest possible thickness sample in the simulation or experiment. Even in the case of a small thickness sample, it can be very difficult to choose the correct branch from the frequencies close to the resonance, where n changes rapidly. A common way to choose the correct branch is to start with frequencies far below the resonance where n is close to 1 and calculate n successively by assuming the continuity of n as the frequency increases. The effective permittivity ,ε_{eff} and the permeability, μ_{eff} can be obtained by $\varepsilon = \frac{n}{Z}$ and $\mu = nZ$. We have employed the retrieved procedure to obtain the effective parameters. But for that aim we need to extract the

transmission and reflection values from simulation. The dimension of proposed design is shown in Table 3.1. It contains a SRR and a backside metalized wire with 1.2 mm width.

Table 3.1. Dimension of proposed meta-material structure.

Design	3
R_{out} (mm)	3.6
w (mm)	0.9
R_{in} (mm)	1.9
g (mm)	0.2
t(μm)	14
FR4 thick (μm)	130

The S parameters are simulated by using HFSS, full-wave electromagnetic software. For HFSS simulation the boundary condition builds up the magnetic excitation. So the PEC is formed along the y direction (gap), PMC is perpendicular to the gap (z direction) and propagation forming across the gap (x direction).
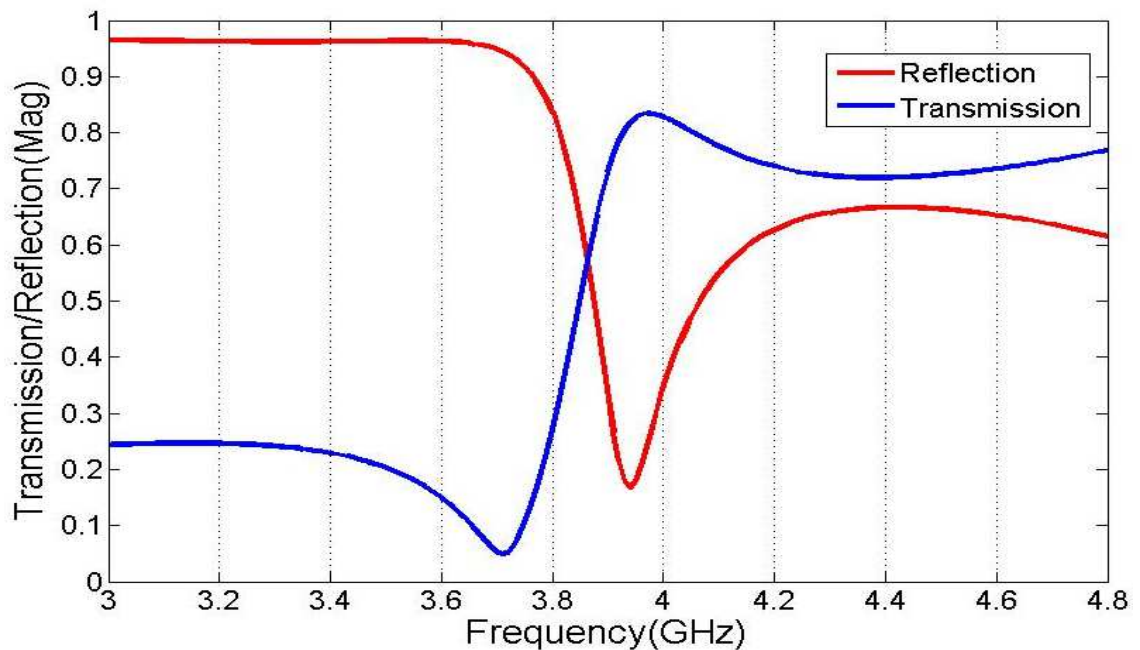
Figure 3.1. Simulated S parameters of proposed Metamaterial design, S11 (Reflection-red line) and S12 (Transmission-blue line).

Transmission (blue line) and Reflection (red line) spectra of a single unit cell of a LHM are plotted in Figure 3.1. The transmission peak and reflection deep appear at 3.89 GHz. As it can be seen the behavior of this structure is reversed in comparison with the alone SRR spectrum. Also we cannot deduce that this is a Metamaterial till we extract the effective parameters especially the refractive index, n. The S parameter data are used to extract impedance, permittivity, permeability and refractive index as shown in Figure 3.2 to Figure 3.5.

Figure 3.2. Extracted Impedance, Re(Z) (red-line) and Im(Z) (blue-dash).

Figure 3.3. Extracted effective permittivity, Re(ε) (red-line) and Im(ε) (blue-dash).
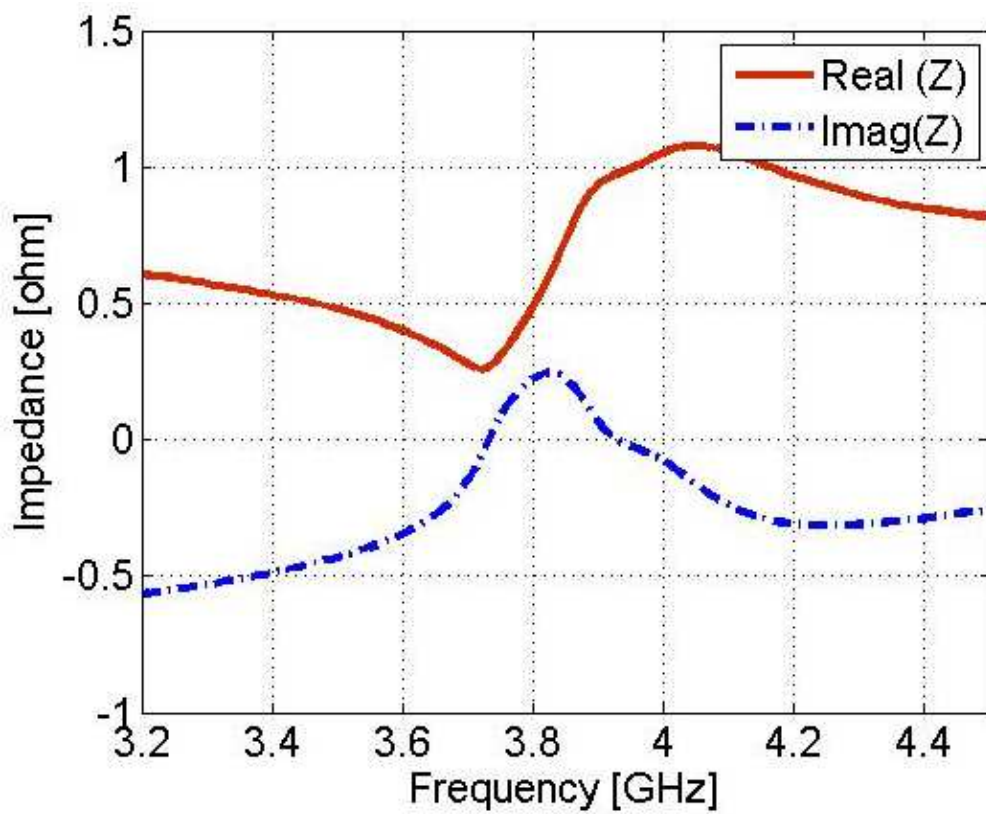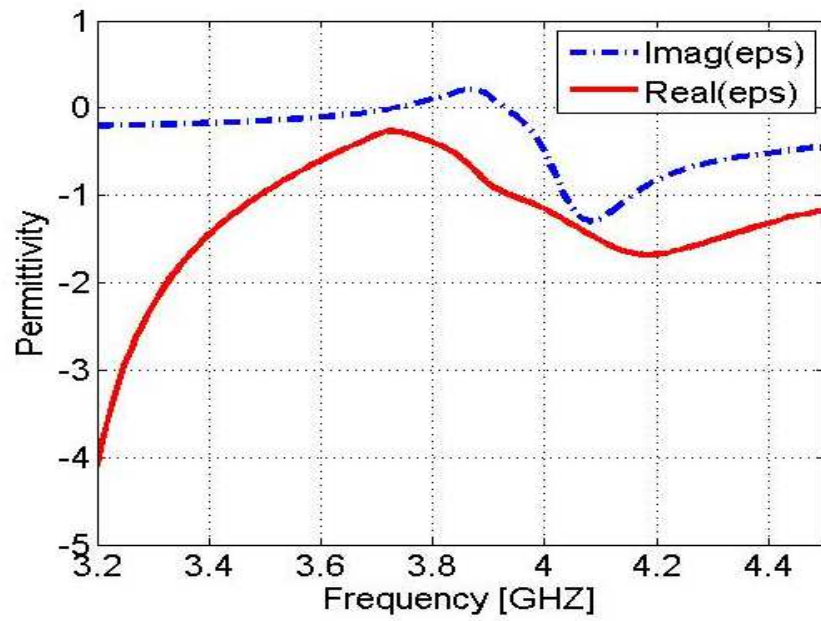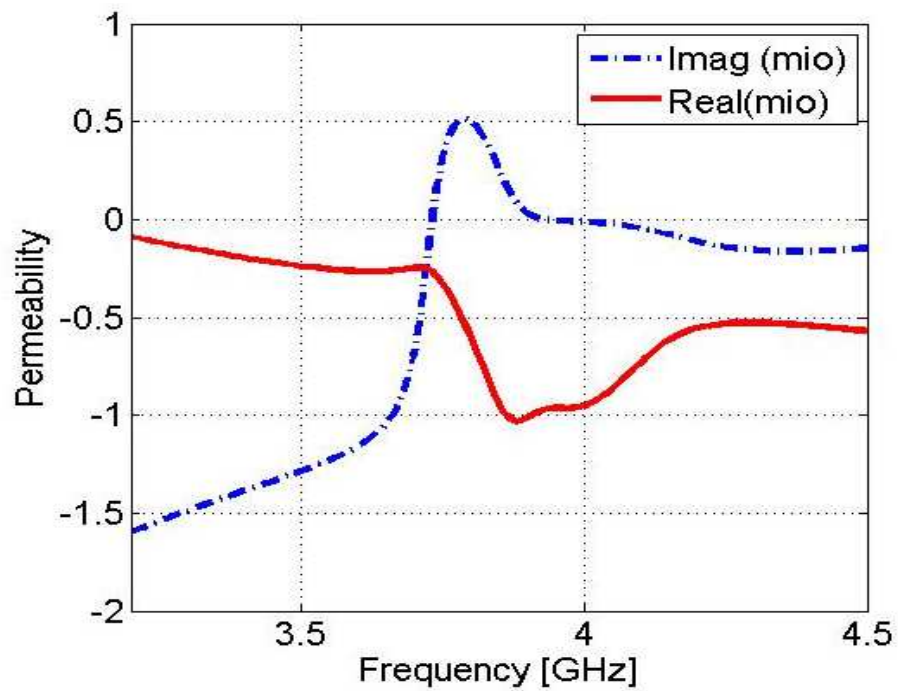

Figure 3.4. Extracted effective permeability, Re(μ)(red-line) and Im(μ) (blue-dash).
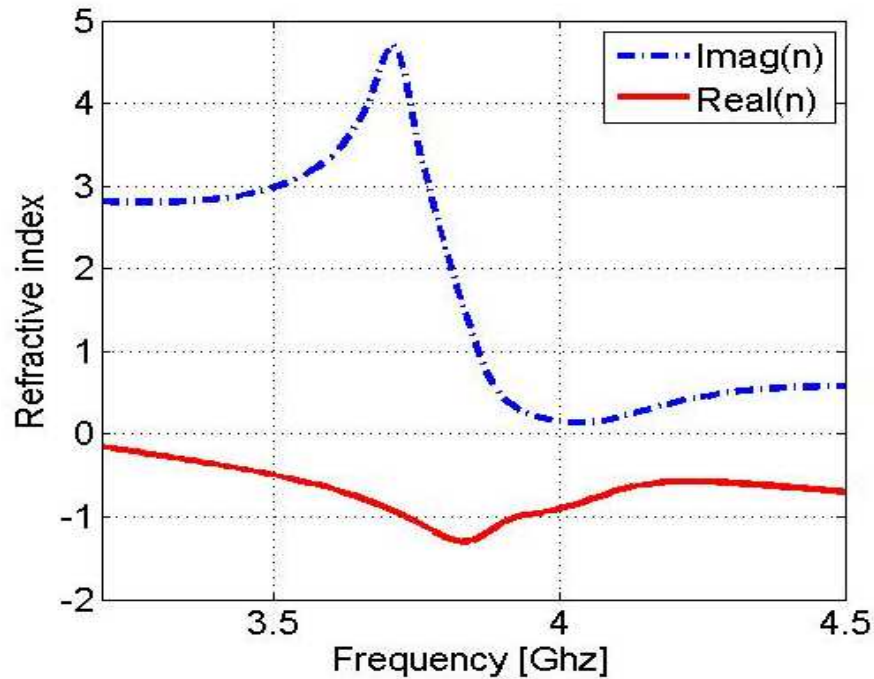
Figure 3.5. Extracted refractive index, Re(n)(red-line) and Im(n) (blue-dash).

3.3.   Absorbing and Heating

Metamaterial surfaces can be conceptualized by periodic arrangement of many small structures. These artificially structures can indeed be regarded as frequency selective surfaces, are influenced by the shape and geometries. The surface is chosen among a conductive material which has a impedance or resistivity around zero. What makes Meta-material interesting for absorbing is in an especial frequency these impedance goes to very large numbers make the surface as absorber structure in that wavelength of incident wave.

3.3.1.   Application of Induced Current

In magnetic excitation where the magnetic field is perpendicular to the gap, the magnetic field induced a circular current on the surface of the SRR. As we discussed above this circular current at the resonance frequency while the SRR shows a huge amount of impedance, make to increase the temperature of the surface. In Figure 3.6 the current on the surface of a Metamaterial has been shown. The average amount of surface current is 5.3 [A- per-m].
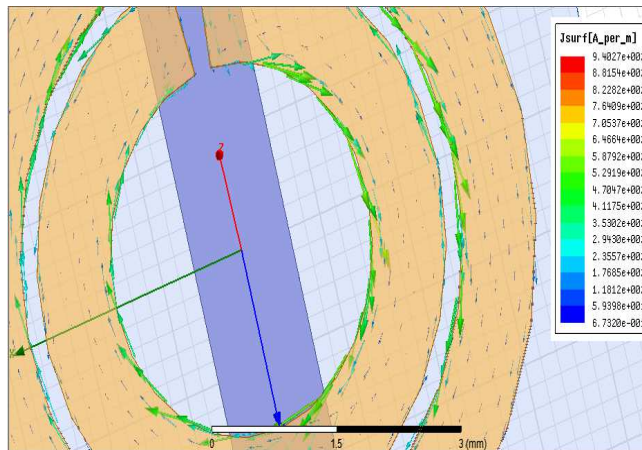
Figure 3.6. Presence of circular current on the surface of Metamaterial.

This amount of increased temperature is one of the major points in high frequency imaging application which may cause the deflection of mirrors.
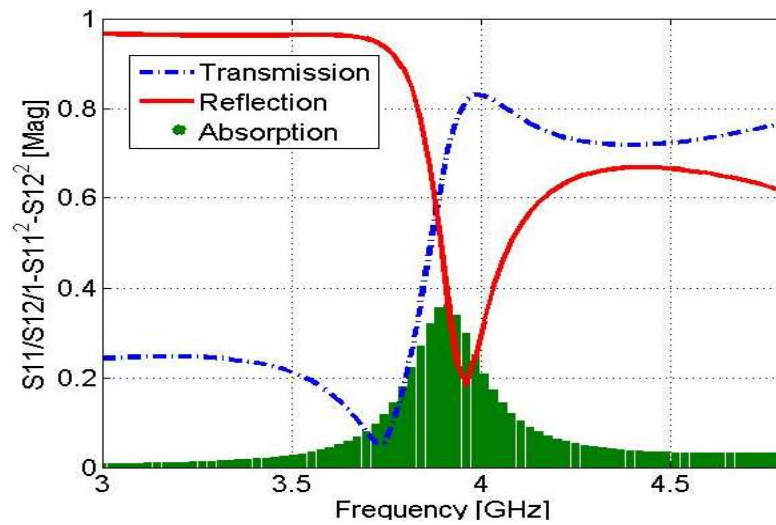
Figure 3.7. Transmission, Reflection and absorption of designed Metamaterial.

The amount of incident wave that neither reflected nor transmitted is absorbed in the structure so $Absorption = 1 - T^2 - R^2$. Here the magnitude of transmission and reflection is considered. Figure 3.7 depicts the absorption quantity of proposed design under simulation condition. It can be seen that when the transmission and reflection get both minimum values simultaneously the absorption of structure goes maximum. An amount of 40% of incident wave is absorbed in the frequency of 4 GHz.

4. EXPERIMENTS AND RESULTS

In this chapter, we will measure the Transmission and reflection spectrum of all fabricated designs (See Table 3.1) in addition to HFSS simulations and equivalent circuit modeling results. The measurements are done with a pair of horn antennas also patch antennas in a certain distances. As like as HFSS simulation we need to be sure about PML boundary condition. Due the SRR unit cells is designed to resonate in 3.6, 4.3, 5.9 and 7.4 GHz measurements are carried on over the [3-8] GHz frequency band. For more measurement we also did a series of experiments on array form of SRR with same sizes also different sizes to broaden the frequency band. The measurement for meta-material design has been done. All the measurement results are plotted with the results achieved with HFSS to make the comparison.

4.1. Analysis and Measurements of the SRR Unit Cell

As discussed earlier for the best characterization of SRR and understand their behavior we need to measure the S parameters to obtain the transmission and reflection information. The measurements have been done in AFM lab using a Network Analyzer (R & S 40GHz). We used a series of horn and patch antennas to sure about the measurement results. For the first step a SRR unit cell for all designs are characterized. Figure 4.1 shows the one unit cell of microwave scale sample with the coordinate system of fields.
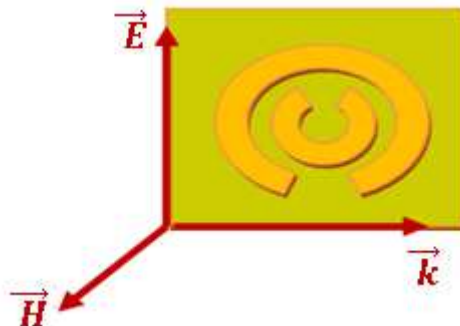
Figure 4.1. Schematic representation of one unit cell of the SRR structure and contributed fields coordinate system.

4.1.1. Measurement Setup

The measurement setups for verifying the S_{11} and S_{12} are shown in Figure 4.2. In the transmission measurements, the microwaves were incident normal to the sample surface, as shown in Figure 4.2. Transmission measurements were calibrated to the transmission between the horns with the sample removed. The reflection measurements were done by placing just one antenna as the source. The reflection measurement was calibrated using a sample-sized sheet of copper as reflecting mirror. In both measurements, the propagation direction was polarized across to the gap.
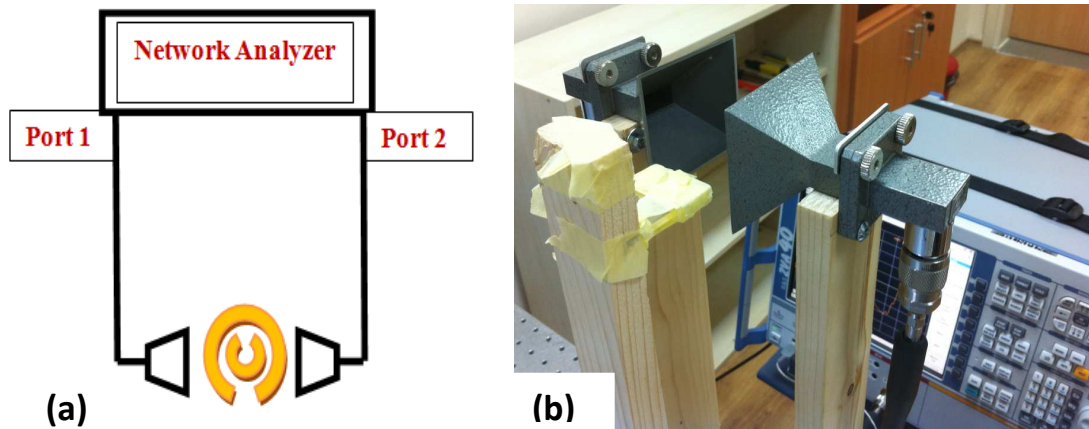
Figure 4.2. The experiment setup for the transmission measurement. (a) Schematic (b) Photograph.

After extracting the S parameters from network analyzer and do the calibration for achieving the transmission and reflection coefficient they are plotted together with results from numerical simulation. The simulated and measured transmission and reflection spectra are shown in Figure 4.3 to Figure 4.5.

Figure 4.3. Plotted S parameters for number 4 design (4 mm radii) (a) Transmission, (b) Reflection spectrum. Red-line shows the extracted data from network analyzer and blue-dash is the HFSS result.

For design number four, as the dimensions gathered in Table 2.1 simulation tool predicts resonance frequency will be at 3.69 GHz. The fabricated sample in measurements shows the resonance behavior almost matches at 3. 69 GHz. In the Figure 4.3b the reflection spectrum can be seen which is match with simulation results.

Figure 4.4. Plotted S parameters for number 3 design (3.6 mm radii) (a) Transmission, (b) Reflection spectrum. Red-line shows the extracted data from network analyzer and blue-dash is the HFSS result.

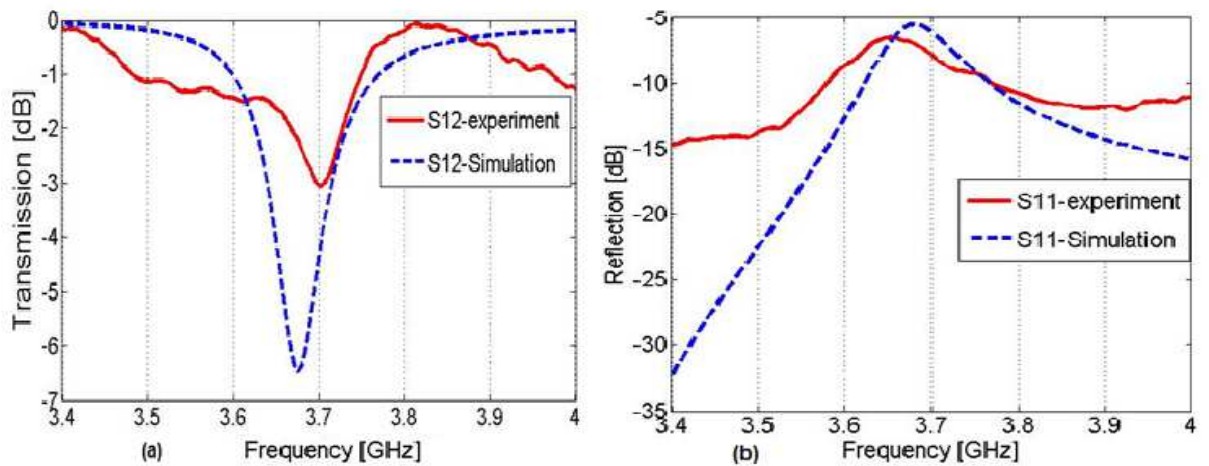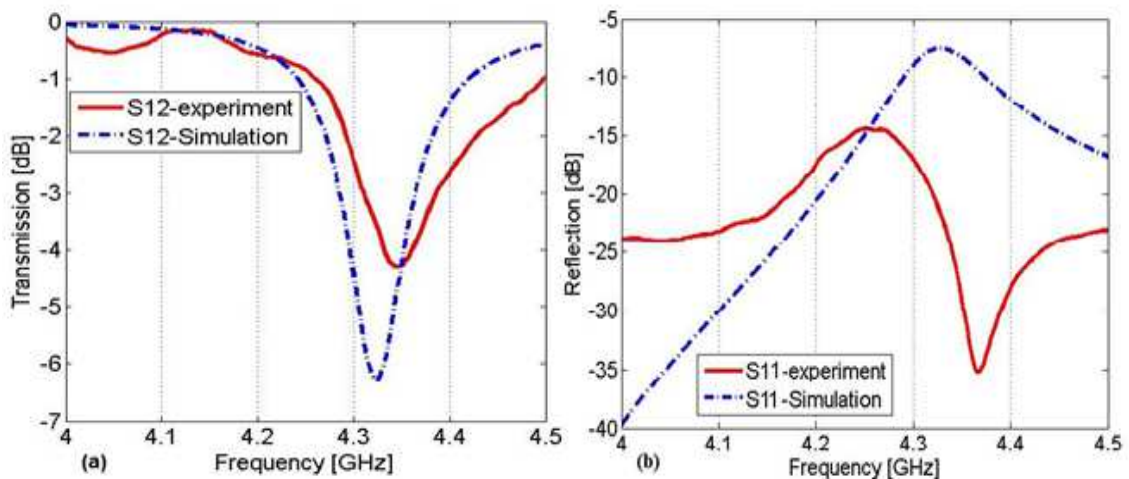For design number three, which has 3.6mm radii simulation tool predicts resonance frequency will be at 4.31GHz. The fabricated sample in measurements shows the resonance behavior almost matches at 3. 35GHz. In the Figure 4.4b the reflection spectrum can be seen which is match with simulation results. There is -15dB reflection from sample at resonance frequency. The dip in reflection spectra comes from antenna characteristics.
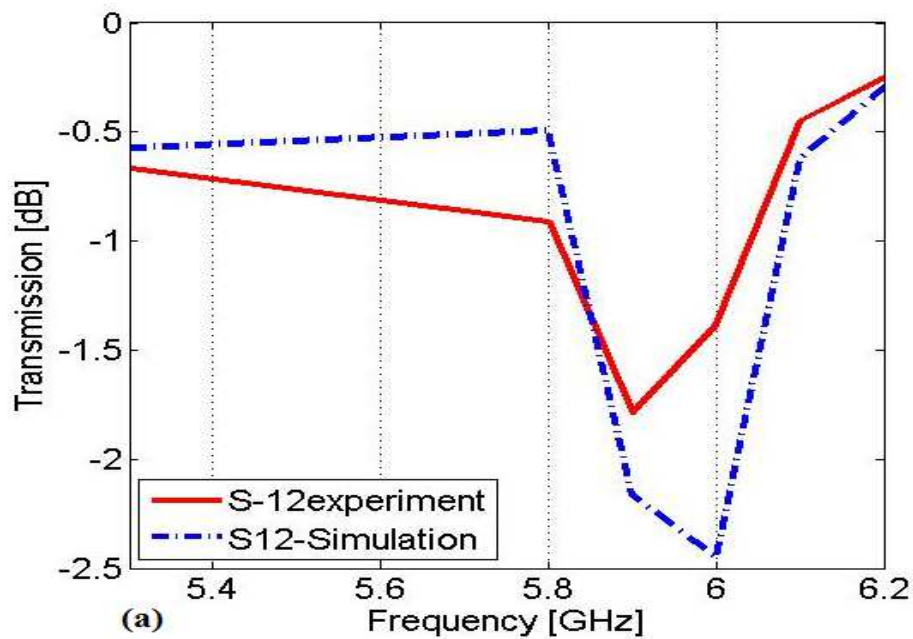
Figure 4.5. Plotted S parameters for number 2 design (3 mm radii) (a) Transmission spectrum. Red-line shows the extracted data from network analyzer and blue- dash is the HFSS result.

It is obviously seen that there is a good match between numerical simulation and measurements results. -2dB attenuation from transmitted power between ports can be seen at 5.9GHz. These experiments have been done for several times with different types of antennas for getting more realistic conclusion.

4.2. Analysis and Measurements of the SRR Array

In this section we will study the effects of neighbored unit cells, in detail if they can influence the amount of capacitances and inductance so the frequency band of the other SRR which are in the vicinity of each other. The ring with 3.6mm radii (design number 3)

is chosen for the array measurements. For the first step 2x1x1 array is characterized. The schematic of 2x1x1 array is shown in Figure 4.6.
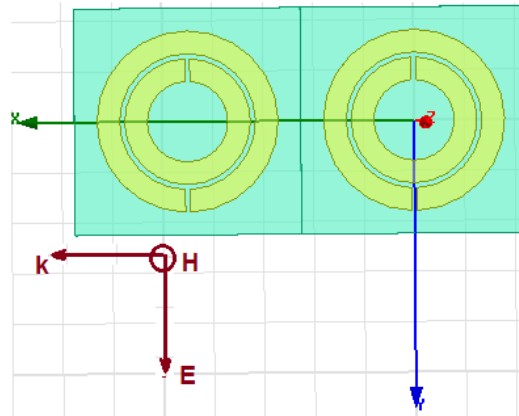
Figure 4.6. Schematic of 2x1x1 array. The radius of outer ring is 3.6mm and the lattice constant is 9mm. The direction of fields and propagation vector is shown.
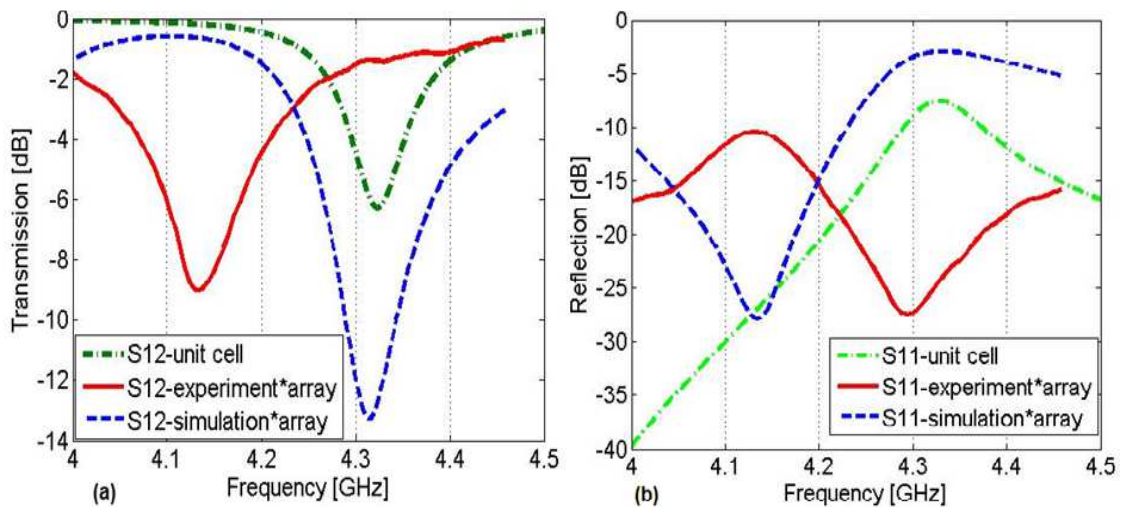
Figure 4.7. Plotted S parameters for 2x1x1 array. (a) Transmission, (b) Reflection spectrum. Red-line shows the extracted data from network analyzer and blue- dash is the HFSS result the S parameters of single unit cell also are shown in green dot-dash.

Also there is a much small difference between the resonance frequency for one unit cell and array but the amplitude of dip (Transmission spectrum) and peak (Reflection spectrum) is more higher that for 2x1x1 array. This difference is obvious for measurement data (red -line) which proves that there is a coupling factor between neighbor cells so increases the overall capacitance so decreasing the resonance dip/peak almost 5%. The

amount of transmitted power in array form is decreased by 40%. The under test device shows similar behavior for reflection spectrum.

4.2.1.   Measurement of the 2x2x2 SRR Array

Combining two arrays of 2x1x1 and 2x1x1 in Y direction and two arrays of 2x1x1 and 2x1x1 in Z direction, it is possible to form a 2x2x2 array. The geometry and dimensions are the same with 2x1x1 array. Figure 4.8 shows the transmission spectrum.
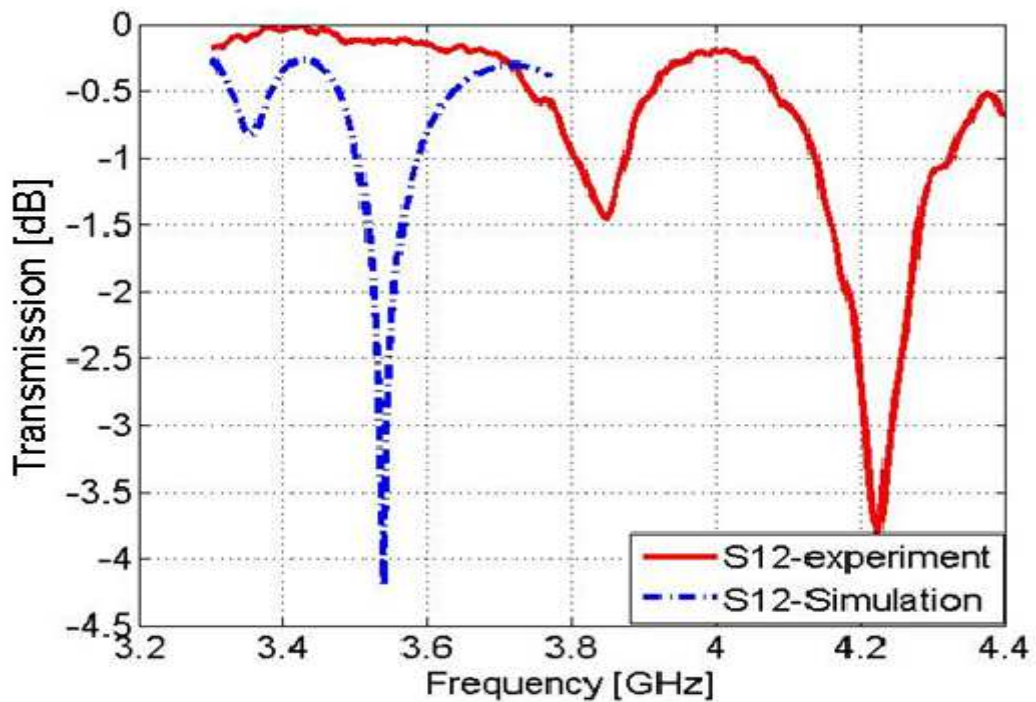
Figure 4.8. Plotted S parameters for 2x2x2 SRR Array transmission. Red-line shows the extracted data from network analyzer and blue-dash is the HFSS result.

What is important in array form of SRRs is the effects of neighboring cells on each other. So as the capacitances between the array rows increase we expect an amount of decrease in resonance frequency. So the first dip in spectrum Figure 4.8 can represent the resonance related to coupling capacitor between layers. And also the second dip is because of the structure parameters around 4.3 GHz.

4.2.2. Measurement of the 2x2x3 SRR Array With Different Sizes of SRRs

Most important thing this section deals with is what does happen if we put for each layer of 2x2x2 array a specified row of SRRs that is different in size with the other layers. What we expect is to have different peaks/dips in reflection or transmission spectrum for each SRR relates to its dimensions which means the broaden resonator. At first layer we put number 3 design (f_m = 4.3 GHz), for second layer we put number 2 design (f_m = 5.9 GHz) and for third layer we put number 1 design (f_m = 7.4 GHz).
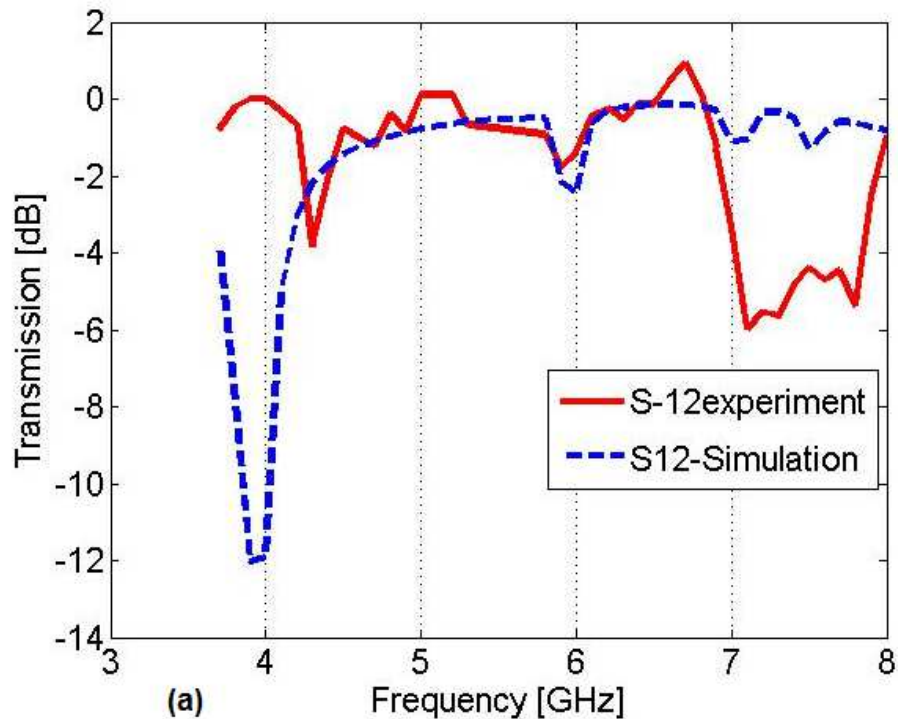
Figure 4.9. Plotted S parameters for 2x2x3 SRR Array with different sizes of SRRs transmission spectrum. Red-line shows the extracted data from network analyzer and blue-dash is the HFSS result.

As it comes from Figure 4.9 there are 3 dips in transmission spectrum each relates to one of the SRRs depending on their sizes. First one is in 4.1 GHz second one is in 5.9 GHz and the third one is between 7.1 and 7.8 GHz. The interesting point in measurement data is the broaden band for third resonance. There is also another resonance dip at 7 GHz in simulation spectrum which comes from the capacitance effects of the layers. It also can comes from antenna characteristics that we did the measurements.

4.3.   Measurement of the Backside Metalized SRRs

Back side metallization of fabricated SRRs wants just one more step of fabrication. So with designing proper width of backside metal the metamaterial structure achieved. The geometrical and numerical simulation was discussed before in detail. Here the measured spectrum is shown.
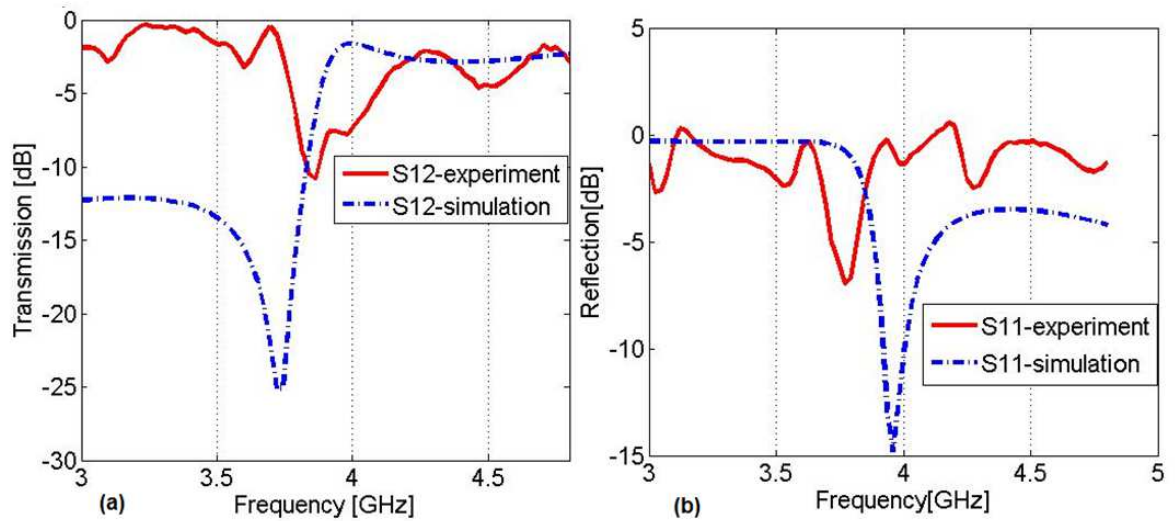
Figure 4.10. Plotted S parameters for Meta-material design (3.6 mm radii) (a) Transmission, (b) Reflection spectrum. Red-line shows the extracted data from network analyzer and blue-dash is the HFSS result.

For Metamaterial structure, as the dimensions gathered in Table 3.1 simulation tool predicts resonance frequency will be at 3.7 GHz. The fabricated sample in measurements shows the resonance behavior almost matches at 3. 75 GHz. In the Figure 4.10b the reflection spectrum can be seen which is almost match with simulation results.

5. THz DESIGN

The existence of SRR that was introduced by Pendry is proven in just microwave regime experimentally. By increasing the studies for NIM (negative index materials) the combination of SRR and wires get more interests. The widespread application they proved can be used in medicine or disclosing the hidden objects increase the researches for tuning the NIM frequencies up to tera-hertz or optical frequencies. Among the papers at terahertz frequencies, Yen *et al*. achieved magnetic response at 0.8–1.3 THz in the planar microstructure SRR composites as measured by spectroscopic ellipsometry [26]. It is predicted that numerous applications will thrive within the THz frequency range.
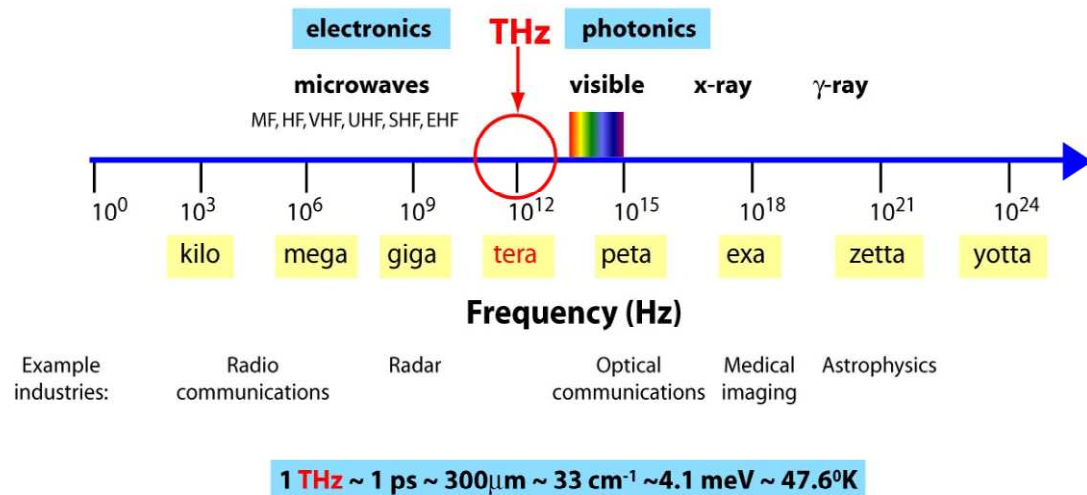
Figure 5.1. Terahertz gap after [34].

Terahertz (THz) spectrum lies between the infrared and microwave spectra covering approximately 0.1 to 10 THz. It is shown that the terahertz Metamaterial has a perfect absorption characteristics also it is perfect for imaging purposes. In continue our fabricated design in microwave frequency is scaled to get a magnetic resonance frequency around 0.3 THz. The material of conducting part is the same but for substrate part we need to choose an appropriate material works in THz frequency band. Our design will be verified by an analytical model the simulation results show a good match with model. Also the behavior of structure will be studied under the oblige incident for understanding the best way of exciting the unit cell.

5.1. Analytical Approach

The schematic of THz design and the parameters are shown in Figure 5.2 and Table 5.1. As similar to microwave design here we will discuss on magnetic response of the SRR. The substrate is chosen Parylene-N with 20 µm thickness.

Table 5.1. Dimension of proposed THz design.

Design	1
R_{out} (µm)	32
w (µm)	4
R_{in} (µm)	26
g (µm)	4
t(µm)	0.1
Substrate thick (µm) h	20

Figure 5.2. THz design on Parylene.

Parylene, discovered in the middle of past century, is the generic name of a family of polymers that has 20 variants, yet only three of them are most commonly used, Parylene N, C, and D. Due to its excellent mechanical, physical, electrical, and barrier properties, Parylene is widely used in many areas, such as nanotechnology, electronics, medical and Pharmacopoeia industries [35]. It gets more attention when the stability and low loss characterization is needed in high frequencies. Also because the application of THz absorber may utilize in human body the compatibility of the material with human body is essential. In this section we prove that the SRR structure made on Parylene substrate has a strong magnetic resonance around 0.32 THz. The dielectric constant of 20 µm Parylene

substrate for this range is 3.5 and the loss tangent is 0.12 [35]. For achieving the model of this structure in addition to all equations (Equation 2.6 to Equation 2.36) which give us the lumped capacitors, inductors and resistors, we need to consider the effects of the fringing capacitance. This capacitance appears because of the penetration of some part of electric field into the substrate. This fringing-field capacitance depends upon the effective permittivity and thickness of the substrate that exist beneath the SRR elements (substrate). Effective dielectric constant can be drawn [36] :

$$\varepsilon_{eff} = \frac{\varepsilon_r + 1}{2} + \frac{\varepsilon_r - 1}{2}\sqrt{1 + 10h/w} \qquad (5.1)$$

Where ε_r is the dielectric constant and h is thickness of substrate. w is the width of strips. Considering the rings of SRR as strip lines, so there is a fringing capacitance between the strip and substrate separately as shown in Figure 5.3.
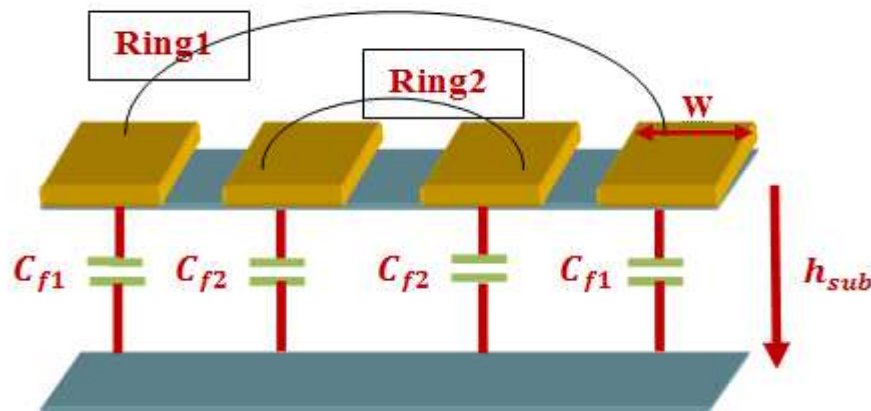

Figure 5.3. Cross section of SRR and representation of fringing capacitances.

We can write the fringing capacitances equation as:

$$Z_0 = \frac{120\pi}{2\pi\sqrt{\varepsilon_{eff}}}\ln\left(\frac{8h}{w} + 0.25w/h\right) \qquad (5.2)$$

Equation 5.2 defines the characteristic impedance of a micro strip line with the same ratio of w/h.

$$C_f = \frac{1}{2}\frac{\sqrt{\varepsilon_{eff}}}{cZ_0} \tag{5.3}$$

$$C_{f'} = \frac{C_f \sqrt[4]{\varepsilon_0/\varepsilon_{eff}}}{1 + A(h/s)\tanh(10s/h)} \tag{5.4}$$

$$A = \exp\left[-0.1 * \exp\left(2.33 - 2.53\,{}^{w}/_{h}\right)\right) \tag{5.5}$$

c is the speed of light in the vacuum and s is the gap width here. As it is seen in Figure 5.3 the fringing capacitances for each ring are in series so the total fringing capacitance is $C_{ftotal} = \frac{C_{f'}}{2}$.

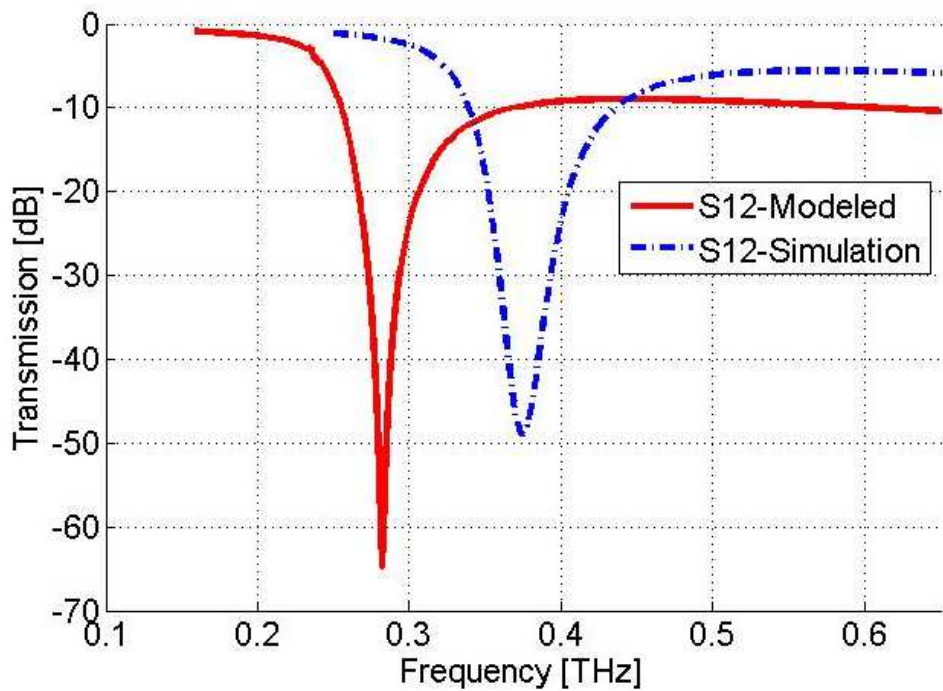Figure 5.4. Plotted Transmission Spectrum for THz design. Red-line shows the extracted curve from analytical model and blue-dash is the HFSS result.

Figure 5.4 shows the differences between modeled result and HFSS simulation. The proposed design has a resonance dip in 0.385 THz and the modeled one shows a resonance frequency at 0.298 THz. Here also there is a mismatch but by considering the ideal cases it can be acceptable.

6. CONCLUSION

The both negative permittivity and permeability materials are artificially structure that have been get attention because of their novelty also widespread application. In summery we studied the basic concepts of LHM which firstly got interests 40 years ago. For that reason after introducing the basic structure of LHM, i.e. split ring resonators as negative permeability media and wire as negative permittivity media in Chapter 1 and 2 we did the retrieved procedure to verify the negativity of refractive index in Chapter 3. The physical concept so, modeling of structures have been considered based on magnetic excitation. In magnetic excitation the electric field makes the SRR as a dipole with different polarization in both sides of gap. So extracting the lumped capacitance and inductance can be done. Simulation results have been completed by HFSS software, simulations which use either PEC/PMC (perfect electric conductor/perfect magnetic conductor) type or perfectly matched layer (PML) type boundary conditions. At Chapter 4 the results of experiment for microwave structures are shown. The measurements have done by a network analyzer named R&S 40GHz and also horn antennas. For getting rid of the side effects of optical table the wooden posts are designed. The experiments have been done in the air so the mode of propagation was TE or TM mode. We need the perpendicular electric field, $\vec{E}$, and magnetic field, $\vec{H}$, both sheer to the propagation direction. Results of numerical HFSS simulations, equivalent circuit model computations and measurements are shown to be in good agreement. This thesis is the first step for validating the good analytical also simulated models for high frequency Metamaterial as future works at THz regime. So Chapter 5 is an introduction for fabrication of THz resonators also future work as THz imagers.

APPENDIX: ANTENNA CHARACTERICTICS

All the characteristics have done by VNA R&S 40 GHz. Antennas measured the transmission power also reflected power in air.
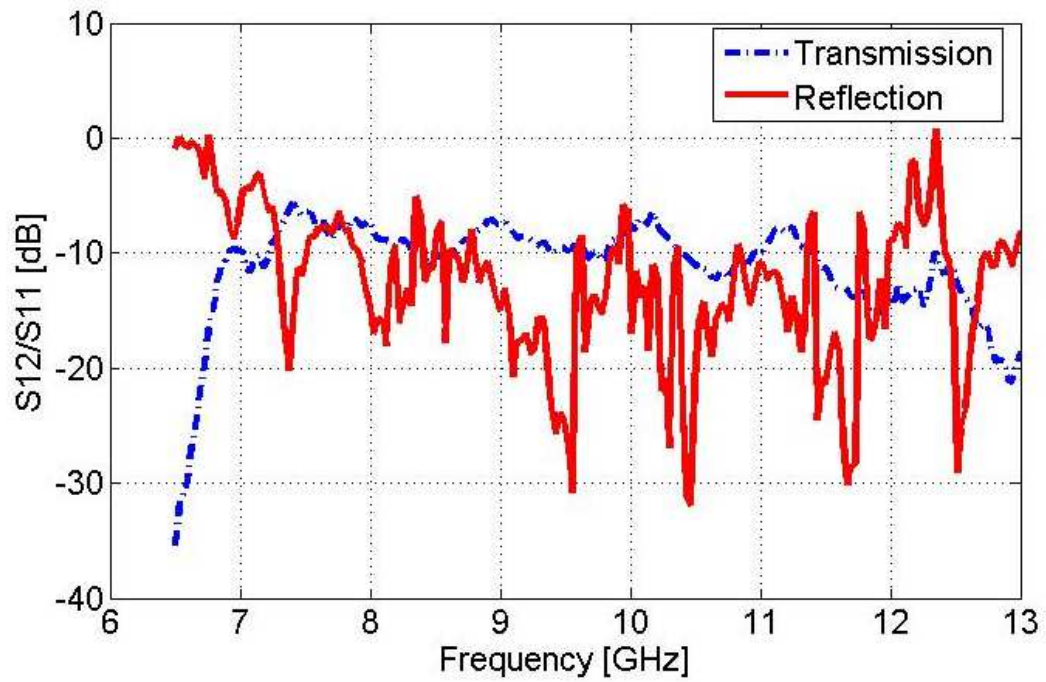

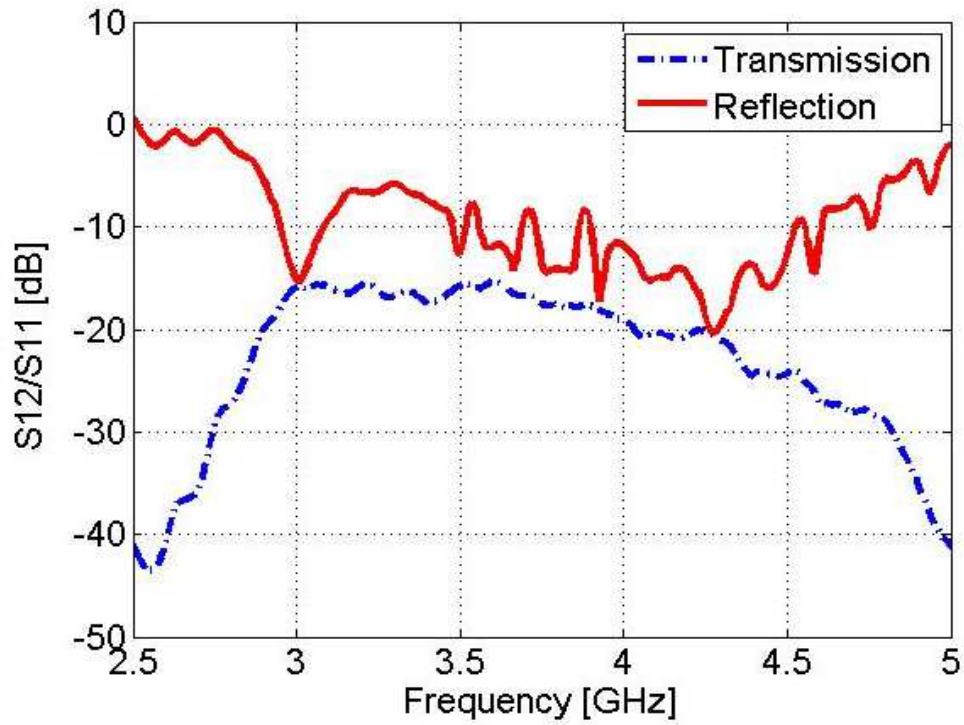Figure A.1. Transmission (blue-dash) and reflection spectrum of horn antennas

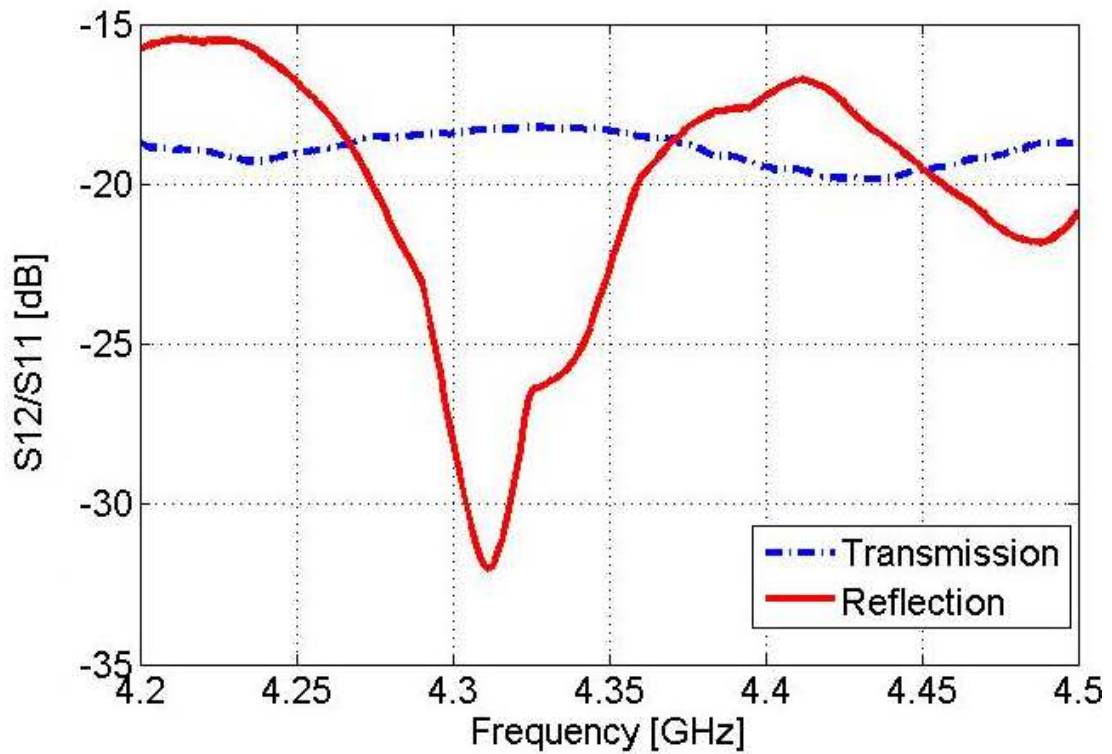Figure A.2. Transmission (blue-dash) and reflection spectrum of commercial antennas.

Figure A.3. Transmission (blue-dash) and reflection spectrum of patch antennas.

REFERENCES

1. Veselago, V. G., "The Electrodynamics of Substances with Simultaneously Negative Values of ε and μ," *Soviet Physics Uspekhi*, Vol. 10, No. 4, pp. 509–514, 1968.

2. Pendry, J. B., A. J. Holden, D. J. Robbins, and W. J. Stewart, "Magnetism from Conductors and Enhanced Nonlinear Phenomena," *IEEE Transactions on Microwave Theory and Techniques*, Vol. 47, No. 11, pp. 2075 –2084, 1999.

3. Katsarakis, N., T. Koschny, M. Kafesaki, E. N. Economou, and C. M. Soukoulis, "Electric Coupling to the Magnetic Resonance of Split Ring Resonators," *Applied Physics Letters*, Vol. 84, No. 15, pp. 2943 –2945, 2004.

4. Marqués, R., "Some Recent Topics in Bulk Split-Ring Metamaterials," presented at the 2nd International Congress on Advanced Electromagnetic Materials in Microwaves and Optics, Pamplona, Spain, 2008.

5. Zhou J., "Study of Left-Handed Materials," PHd, Iowa State University, Ames, Iowa, 2008.

6. Smith, D. R., W. J. Padilla, D. C. Vier, S. C. Nemat-Nasser, and S. Schultz, "Composite Medium with Simultaneously Negative Permeability and Permittivity," *Physical Review Letters*, Vol. 84, pp. 4184–4187, May. 2000.

7. Yen, T. J., W. J. Padilla, N. Fang, D. C. Vier, D. R. Smith, J. B. Pendry, D. N. Basov, and X. Zhang, "Terahertz Magnetic Response from Artificial Materials," *Science*, Vol. 303, No. 5663, pp. 1494–1496, 2004.

8. Katsarakis, N., G. Konstantinidis, A. Kostopoulos, R. S. Penciu, T. F. Gundogdu, M. Kafesaki, E. N. Economou, T. Koschny, and C. M. Soukoulis,

"Magnetic Response of Split-Ring Resonators in the Far-Infrared Frequency Regime," *Optics Letters*, Vol. 30, No. 11, pp. 1348–1350, 2005.

9. Linden, S., C. Enrich, M. Wegener, J. Zhou, T. Koschny, and C. M. Soukoulis, "Magnetic Response of Metamaterials at 100 Terahertz," *Science*, Vol. 306, No. 5700, pp. 1351–1353, 2004.

10. Enrich, C., M. Wegener, S. Linden, S. Burger, L. Zschiedrich, F. Schmidt, J. F. Zhou, T. Koschny, and C. M. Soukoulis, "Magnetic Metamaterials at Telecommunication and Visible Frequencies," *Physical Review Letters*, Vol. 95, No. 20, p. 203901, 2005.

11. Shalaev, V. M., W. Cai, U. Chettiar, H.-K. Yuan, A. K. Sarychev, V. P. Drachev, and A. V. Kildishev, "Negative Index of Refraction in Optical Metamaterials," *Optics Letters*, Vol. 30, No. 24, pp. 3356-3358, 2005.

12. Dolling, G., C. Enrich, M. Wegener, J. F. Zhou, C. M. Soukoulis, and S. Linden, "Cut-Wire Pairs and Plate Pairs as Magnetic Atoms for Optical Metamaterial," *Optics Letters*, Vol. 30, No. 23, pp. 3198–3200, 2005.

13. Zhou, J., L. Zhang, G. Tuttle, T. Koschny, and C. M. Soukoulis, "Negative Index Materials Using Simple Short Wire Pairs," *Physical Review B*, Vol. 73, p. 41101, 2006.

14. Zhou, J., E. N. Economon, T. Koschny, and C. M. Soukoulis, "Unifying Approach to Left-Handed Material Design," *Optics Letters*, Vol. 31, No. 24, pp. 3620–3622, 2006.

15. Dolling, G., C. Enrich, M. Wegener, C. M. Soukoulis, and S. Linden, "Simultaneous Negative Phase and Group Velocity of Light in a Metamaterial," *Science*, Vol. 312, No. 5775, pp. 892–894, 2006.

16. Zhang, S., W. Fan, N. C. Panoiu, K. J. Malloy, R. M. Osgood, and S. R. J. Brueck, "Experimental Demonstration of Near-Infrared Negative-Index Metamaterials," *Physical Review Letters*, Vol. 95, No. 13, p. 137404, 2005.

17. Dolling, G., M. Wegener, C. M. Soukoulis, and S. Linden, "Negative-Index Metamaterial at 780 nm Wavelength," *Optics Letters*, Vol. 32, No. 1, pp. 53-55, 2007.

18. Kafesaki, M., I. Tsiapa, N. Katsarakis, T. Koschny, C. M. Soukoulis, and E. N. Economou, "Left-handed Metamaterials: The Fishnet Structure and Its Variations," *Physical Review B*, Vol. 75, p. 235114, 2007.

19. Katsarakis, N., M. Kafesaki, I. Tsiapa, E. N. Economou, and C. M. Soukoulis, "High Transmittance Left-handed Materials Involving Symmetric Split-Ring Resonators," *Photonics and Nanostructures*, Vol. 5, pp. 149–155, 2007.

20. Davies, A. G., A. D. Burnett, W. Fan, E. H. Linfield, and J. E. Cunningham, "Terahertz Spectroscopy of Explosives and Drugs," *Materials Today*, Vol. 11, No. 3, pp. 18–26, 2008.

21. Anonymous, *Oncology | Terahertz Medical Applications - TeraView,* http://www.teraview.com/applications/medical/oncology.html, Accessed at June 2012.

22. Anonymous, *Passive Standoff Concealed Objects Detection Systems - TS4,* http://www.thruvision.com/Products/TS4_Sub_Pages/TS4_Product_Page.htm, Accessed at June 2012

23. Anonymous, *Ansoft HFSS Online Help*, http://www.scribd.com/doc/45193657/Ansoft-HFSS-Online-Help. Accessed at June 2012.

24. Zhou, J., T. Koschny, and C. M. Soukoulis, "Magnetic and Electric Excitations in Split Ring Resonators," *Optical Express*, Vol. 15, No. 26, pp. 17881–17890, 2007.

25. Chen, C. Y. and T. J. Yen, "Electric and Magnetic Responses in the Multiple-Split Ring Resonators by Electric Excitation," *Journal of Applied Physics*, Vol. 105, No. 12, pp. 124913–124915, 2009.

26. Azad, A. K., J. Dai, and W. Zhang, "Transmission Properties of Terahertz Pulses Through Subwavelength Double Split-Ring Resonators," *Optics letters*, Vol. 31, No. 5, pp. 634–636, 2006.

27. Aydin, K. and E. Özbay, "Experimental and Numerical Analyses of the Resonances of Split Ring Resonators," *physica status solidi (b)*, Vol. 244, No. 4, pp. 1197–1201, 2007.

28. Marqués, F., Medina, and R. Rafii-El-Idrissi, "Role of Bianisotropy in Negative Permeability and Left-Handed Metamaterials," *Physical Review B*, Vol. 65, p. 144440, 2002.

29. Sauviac, B., C. R. Simovski, and S. A. Tretyakov, "Double Split-Ring Resonators: Analytical Modeling and Numerical Simulations," *Electromagnetics*, Vol. 24, No. 5, pp. 317–338, 2004.

30. Sydoruk, O., E. Tatartschuk, E. Shamonina, and L. Solymar, "Resonant Frequency of Singly Split Single Ring Resonators: an Analytical and Numerical study," presented at the 2nd International Congress on Advanced Electromagnetic Materials in Microwaves and Optics, Pamplona, Spain, 2008.

31. Örten, P. Y. , "Numerical Analysis, Design and Two-Port Equivalent Circuit Models for Split Ring Resonator Arrays," Master, Middle East Technical University, Ankara- Turkey, 2010.

32. Ozbay, E., K. Aydin, E. Cubukcu, and M. Bayindir, "Transmission and Reflection Properties of Composite Double Negative Metamaterials in Free Space," *IEEE Transactions on Antennas and Propagation*, Vol. 51, No. 10, pp. 2592 – 2595, 2003.

33. Smith, D. R., S. Schultz, P. Markoš, and C. M. Soukoulis, "Determination of Effective Permittivity and Permeability of Metamaterials from Reflection and Transmission Coefficients", *Physical Review B* , Vol. 65, No. 19, p. 195104, 2002.

34. Anonymous, *CIRCE: Filling the THz Gap*, http://circe.lbl.gov/THzGap.html, Accessed at September 2012.

35. Liu, X., S. MacNaughton, D. B. Shrekenhamer, H. Tao, S. Selvarasah, A. Totachawattana, R. D. Averitt, M. R. Dokmeci, S. Sonkusale, and W. J. Padilla, "Metamaterials on Parylene Thin Film Substrates: Design, Fabrication, and Characterization at Terahertz Frequency," *Applied Physics Letters*, Vol. 96, No. 1, pp. 011906–011903, 2010.

36. Hong J.S. G. and M. J. Lancaster, *Microstrip Filters for RF/Microwave Applications*, John Wiley & Sons, New York, 2001.